Earth and Planetary Science Letters 556 (2021) 116728

Contents lists available at ScienceDirect

Earth and Planetary Science Letters

www.elsevier.com/locate/epsl

The 25 March 2020 M_W 7.5 Paramushir, northern Kuril Islands earthquake and major ($M_W \geq 7.0$) near-trench intraplate compressional faulting

Lingling Ye [a], Thorne Lay [b,*], Hiroo Kanamori [c]

[a] Guangdong Provincial Key Lab of Geodynamics and Geohazards, School of Earth Sciences and Engineering, Sun Yat-sen University, Guangzhou, China
[b] Department of Earth and Planetary Sciences, University of California Santa Cruz, Santa Cruz, CA 95064, USA
[c] Seismological Laboratory, California Institute of Technology, Pasadena, CA 91125, USA

ARTICLE INFO

Article history:
Received 26 September 2020
Received in revised form 8 December 2020
Accepted 16 December 2020
Available online xxxx
Editor: R. Bendick

Keywords:
near-trench intraplate compressional faulting
2020 Kuril slab earthquake
slab bending earthquakes
outer trench slope faulting temporal cycles

ABSTRACT

Large compressional-faulting earthquakes located relatively deep in oceanic lithosphere entering subduction zones are primarily caused by plate bending stress, but their timing, depth extent and size can be influenced by temporally-varying shear stress on the plate boundary. The 25 March 2020 M_W 7.5 event in the Pacific plate seaward of Paramushir Island (northern Kuril Islands), is among the largest recorded events of this type. Its rupture extends along a large-slip region in the southwestern portion of the 1952 Kamchatka M_W 9.0 rupture zone. This region has somewhat lower interplate coupling than the megathrust fault along Kamchatka to the northeast, but there could be 68 yrs of strain accumulation. The 2020 event is considered in the context of the 24 recorded major ($M_W \geq 7.0$) near-trench intraplate compressional-faulting events. An updated compilation of temporally varying near-trench intraslab faulting relative to major interplate ruptures indicates that the stress cycles on the plate boundary influence both extensional and compressional near-trench faulting caused by plate bending. Particularly noteworthy are such events seaward of areas presumed to be in an advanced stage of their seismic cycle, including relatively shallow compressional events along the 1944 M_W 8.1 Tonankai, Japan rupture zone, along with activity along the 1952 Kamchatka and 1922 Chile rupture zones.

1. Introduction

Oceanic plates flex as they converge in subduction zones, with their elastic/brittle near-surface volume experiencing shallow extensional faulting and less common deeper compressional faulting from the outer rise to beneath the overriding plate (e.g., Stauder, 1968; Chapple and Forsyth, 1979; Christensen and Ruff, 1983, 1988; Lay et al., 1989; Seno and Yamanaka, 1996; Craig et al., 2014). The oceanic lithospheric age/thermal state and plate bending curvature that results from slab pull, in-plate normal stress and plate boundary shear stresses influence the depth extent of the seismogenic material and position of the neutral elastic bending stress surface within the flexing lithosphere, respectively. Slab pull and in-plane normal stress load on the oceanic lithosphere from the overriding plate are primarily responsible for the slab bending, but time-varying interplate shear stress arising from stick-slip of the plate boundary is also thought to influence the stresses in the oceanic lithosphere (e.g., Dmowska et al., 1988; Taylor et al., 1996). The downward transition to ductile/plastic deformation in the oceanic lithosphere caused by temperature increase delimits the elastic domain in which compressional faulting can occur (e.g., Chapple and Forsyth, 1979; Craig et al., 2014). As a result, major compressional events within the shallow slab are rare and likely require broadening of the region under compression by shallowing of the neutral surface as a result of build up of plate boundary shear stresses or transient loading by extensive extensional faulting of the shallower elastic lithosphere.

For regions that experience large megathrust earthquakes, the interplate shear stress cycle can temporally modulate the faulting in the oceanic lithosphere. This is indicated by near-trench extensional faulting mainly occurring after large interplate thrust events and infrequent large near-trench compressional faulting being more common before large plate boundary events (e.g., Christensen and Ruff, 1983, 1988; Lay et al., 1989). Purely elastic modeling of stress modulation may overestimate the influence of interplate coupling on the intraplate stresses (e.g., Mueller et al., 1996; Lay et al., 2009), and the depth distribution of faulting mechanisms largely conforms to expectations of elastic-plastic plate bending

* Corresponding author.
E-mail address: tlay@ucsc.edu (T. Lay).

https://doi.org/10.1016/j.epsl.2020.116728

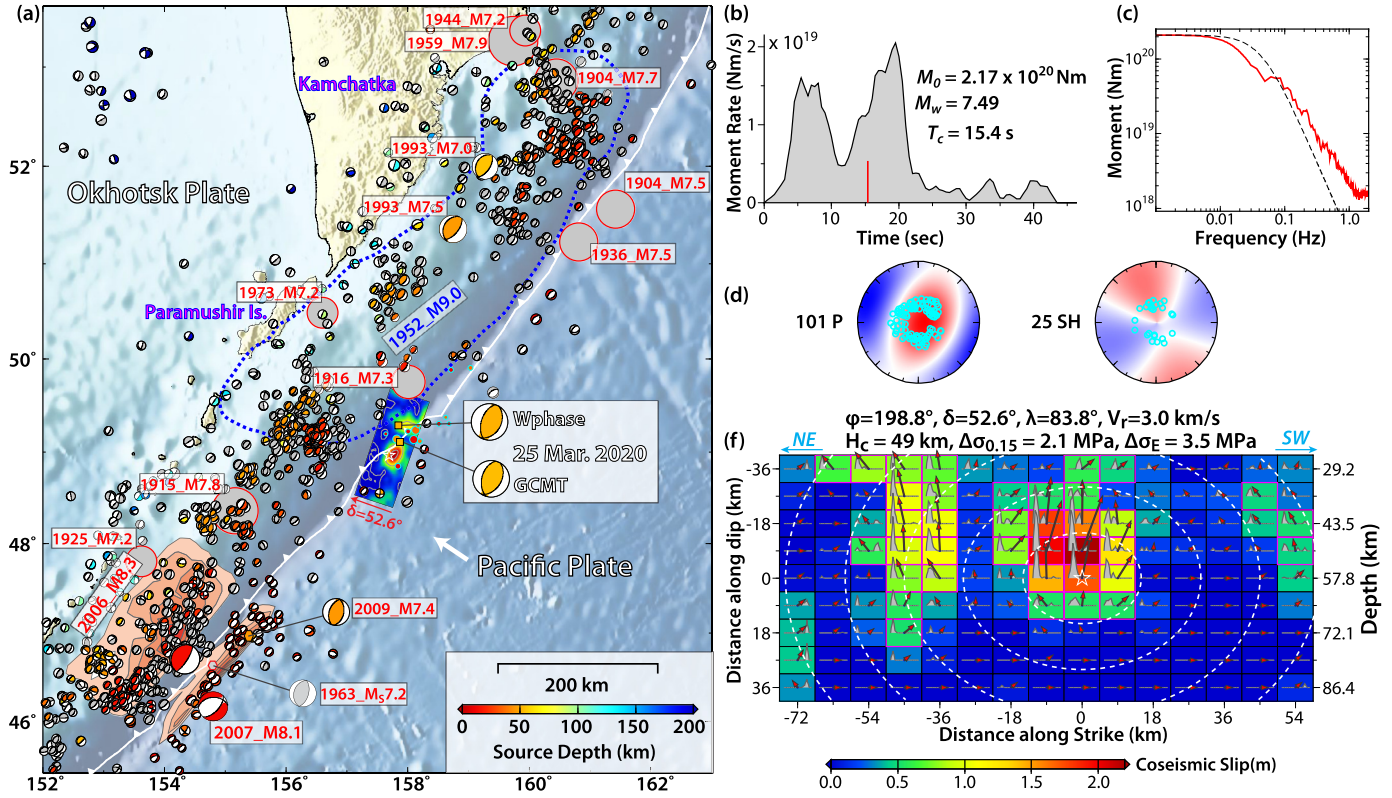

Fig. 1. Rupture location and slip distribution for the 25 March 2020 M_W 7.5 Paramushir, Northern Kuril Islands outer rise compressional earthquake. (a) The Global Centroid Moment Tensor (GCMT) and W-phase solutions for the 2020 event are shown in the highlighted box (centroid depths ~50-53 km). Small circles with cyan outlines show the 3-month aftershock sequence. GCMT solutions for events before the 2006 M_W 8.3 event are shown in gray and those events after the 2006 M_W 8.3 event are color-coded by their centroid depths. Larger mechanisms highlight events with magnitudes ≥7.0. Labeled gray circles show large shallow events with magnitudes ≥7.2 from 1900 to 1976 (USGS-NEIC catalog). The blue dashed curve indicates the aftershock region of the 1952 M_W 9.0 Kamchatka earthquake (MacInnes et al., 2010). The red contoured slip distributions for the 2006 M_W 8.3 megathrust event and 2007 M_W 8.1 outer trench-slope normal faulting event are from Lay et al. (2009). The toothed heavy white line indicates the position of the Kuril trench. (b) The moment-rate function, with a red tick at the centroid time T_c. (c) Source spectrum inferred from the moment-rate function and teleseismic P spectra (red line) and a reference spectrum with stress factor of 3.0 MPa (dashed blue line). (d) Lower-hemisphere stereographic projections of the P-wave (left) and SH-wave (right) radiation patterns with raypath take-off positions for the data used in the inversion. (f) Slip distribution, with arrows showing the magnitude and direction of slip (hanging-wall relative to foot-wall) and subfaults color-coded by peak slip. The dashed blue curves indicate the positions of the rupture expansion front in 5 s intervals. The subfault source time functions are shown within each subfault by gray polygons.

models (e.g., Craig et al., 2014); however, the temporal modulation of shallow extensional activity is unambiguous (e.g., Wetzler et al., 2017; Sladen and Trevisan, 2018).

On 25 March 2020, a major (M_W 7.5) near-trench compressional event struck near the northern Kuril Islands trench seaward of Paramushir Island (Fig. 1) southwest along the arc from the Kamchatka peninsula (USGS-NEIC 02:49:21.16 UTC, 48.964°N, 157.696°E, 57.8 km deep; https://earthquake.usgs.gov/earthquakes/eventpage/us70008fi4/executive). Lower-magnitude intraplate compressional and tensional events have occurred near the source region (e.g., Christensen and Ruff, 1988; Lay et al., 2009; Craig et al., 2014), compatible with flexural bending of the Pacific plate as it subducts. However, the large size and depth of the 2020 event raises the possibility that the intraplate compressional stress regime may be augmented by increasing shear stress on the nearby megathrust fault, broadening the vertical extent of the elastic/brittle compressional domain and enabling such a large intraplate event to occur. We examine the rupture of this event and consider it in the context of rare major ($M_W \geq 7.0$) near-trench intraplate compressional events along with updating a global compilation of temporal behavior of near-trench tensional and compressional activity relative to major interplate ruptures. We note several regions, including the 1952 Kamchatka zone, for which outer rise compressional activity may indicate accumulating plate boundary stress associated with forthcoming major interplate thrust-faulting.

2. The 25 March 2020 Paramushir earthquake

We performed seismic analyses of the 2020 Paramushir earthquake. A point-source moment tensor solution is obtained by W-phase inversion (e.g., Kanamori and Rivera, 2008) and the slip distribution is obtained by a kinematic finite-fault inversion of teleseismic P and SH waves (e.g., Hartzell and Heaton, 1983; Kikuchi and Kanamori, 1991; Ye et al., 2016).

2.1. W-phase inversion

We perform a W-phase inversion using 203 broadband waveforms from 94 global stations, filtered in the passband 0.002 to 0.005 Hz. The solution found after a grid search over source depth and centroid location is shown in Fig. 1. The scalar moment is 2.10×10^{20} Nm (M_W 7.48), with the best double-couple nodal planes having strike, $\phi_1 = 198.8°$, dip, $\delta_1 = 52.6°$, and rake, $\lambda_1 = 84°$, and $\phi_2 = 28.6°$, $\delta_2 = 37.8°$, and $\lambda_2 = 97.8°$, for a source depth of 50.5 km. The solution has an 11.1 s centroid time shift and a centroid location at latitude = 49.290°N, longitude = 157.850°E. The centroid location is dependent on the PREM velocity model, so it may not correspond to the true centroid of the slip distribution. The W-phase solution is similar to that for the Global Centroid-Moment Tensor (GCMT) solution, which has a scalar moment of 2.07×10^{20} Nm, source depth of 52.6 km, centroid time shift of 10.9 s, and best double-couple nodal planes having $\phi_1 = 194°$,

$\delta_1 = 48°$, and $\lambda_1 = 78°$, and $\phi_2 = 32°$, $\delta_2 = 43°$, and $\lambda_2 = 103°$ (https://www.globalcmt.org/CMTsearch.html).

2.2. Finite-fault inversion

We perform finite-fault slip inversions of teleseismic broadband P and SH waveforms for both candidate fault planes from the best double-couple geometry of our W-phase moment tensor (as well as a range of other geometries including the GCMT solution). A simple 1D velocity model based on model Crust1.0 with a uniform water layer 6.17 km deep (Laske et al., https://igppweb.ucsd.edu/~gabi/crust1.html) is used for the source region structure. 101 broadband P waves and 25 broadband SH waves with stable waveforms filtered in the passband 0.005 to 0.9 Hz with excellent azimuthal coverage are included in the inversion (Fig. 2). A kinematic rupture expansion velocity of 3.0 km/s is used for the preferred model (models for a range of rupture velocities from 2.5 to 3.5 km/s were computed), with subfault source time functions parameterized with 10 1.5-s rise-time triangles offset by 1.5-s each, allowing up to 16.5 s subfault durations. Models are parameterized with 15 9-km-long subfaults along strike and 9 7.5-km-wide subfaults along dip, with the hypocenter set at the USGS-NEIC depth of 57.8 km. The 3.0 km/s expansion velocity is not tightly constrained by the data, but higher values lead to increasingly patchy slip distribution, which may be unrealistic. The location of the event within the subducted lithosphere is compatible with rupture velocity being higher than typical of interplate events (e.g., Ye et al., 2016). For example, a rupture velocity of 3.5 km/s was preferred for the 13 January 2007 M_W 8.1 near-trench intraplate rupture located to the southwest (e.g., Lay et al., 2009).

The inversions for the northwest-dipping fault account for ~80% of the power in the teleseismic waveforms, and give ~6% better residual waveform power reduction than for the northeast-dipping fault. This is greater improvement in fit relative to that found (<2%) for perturbations of rupture velocity, subfault duration, and precise geometry of the northwest-dipping fault. Fig. 1 shows a corresponding inversion for $\phi = 198.8°$, $\delta = 52.6°$. The resulting slip model has a primary slip patch extending from 29 to 65 km, with peak slip of ~2.2 m, near the hypocenter (Fig. 1f). The down-dip extent of slip is constrained well by the data. Weak slip late in the source process has poor depth resolution because uncertainty in the Green's functions increases with time into the rupture. This model has a slip-weighted average stress drop of 3.5 MPa and circular area-based stress drop of 2.1 MPa (following the procedure in Ye et al., 2016; Fig. S1a), with individual subfault source time functions generally indicating simple, short duration radiation. The moment-rate function is most reliable for the first 25 s and is then followed by minor late pulses that are not well resolved (Fig. 1b). Comparison of the observations and predictions from this model shows that the first ~50 s of the P and SH signals are well modeled and that there is minor northeastward directivity in the waveforms (Figs. 1c and 2), accounted for by a secondary slip patch about 40 km to the northeast from the hypocenter 15 s after the rupture onset.

Results for an inversion using the alternate, southeast-dipping candidate fault plane, with $\phi = 28.6°$, $\delta = 37.8°$, are presented in Figs. S1b, S2, and S3. The overall waveform power misfit is 6% larger for this geometry relative to that in Fig. 1, and there is also relatively poorer fitting of the depth phases for those stations to the west highlighted by gray in Figs. 2 and S3. These data are not perfectly fit for the northwest-dipping fault plane choice either, suggesting that the Green's functions for the depth phases do not fully account for the complex shallow propagation through the wedge and dipping bathymetry landward from the event for the western azimuth range. The USGS-NEIC preferred finite fault solution uses a similarly oriented southeastward dipping fault with strike of 29° and dip of 43°, and has a main slip patch with slip of up to 4 m near the hypocenter and a secondary slip patch ~25 km to the northeast (https://earthquake.usgs.gov/earthquakes/eventpage/us70008fi4/finite-fault). The slip distribution is similar to our model in Fig. S2. There is not great sensitivity to the choice of fault plane overall, but we prefer the northwest dipping solution in Fig. 1 based on the overall improvement in waveform fitting.

No immediate foreshocks were detected near the hypocenter by the USGS-NEIC, and aftershocks within 30 days with magnitudes of 4.1 to 5.2 extend ~75 km northeastward along the trench strike, with depths ranging from 27 to 44.6 km. The catalog locations of aftershocks do not resolve the choice of fault plane.

2.3. Location relative to the 1952 Kamchatka event

The Paramushir event is located beneath the trench offshore of the southwestern end of the 1952 M_W 9.0 Kamchatka rupture (Fig. 1). The southwestern extent of that great event is not tightly constrained by rupture analysis, but aftershock locations extend southwestward to offshore of Paramushir (e.g., Gusev, 2006; Kelleher et al., 1973; Kelleher and Savino, 1975; Fedotov et al., 1982). Tsunami modeling of both far-field and near-field observations indicates that very large slip occurred offshore of the island during the 1952 event (e.g., Johnson and Satake, 1999; MacInnes et al., 2010). GPS measurements along the Kuril Islands are sparse, but do include a station on northern Paramushir. It shows ~6 mm/yr of northwestward motion (Steblov et al., 2010), which is ~40% of the peak northwestward velocities along Kamchatka (Bürgmann et al., 2005). Lacking GPS sites in the central Kuril Islands, the interplate coupling is uncertain, but Steblov et al. (2010) model the available observations with laterally reducing coupling reaching a minimum near 49°N. The megathrust southwest of the 2020 event may be weakly coupled to near the 2006 M_W 8.3 shallow interplate rupture zone (Fig. 1), along which subsequent intensive trench slope intraplate activity occurred, including the 2007 M_W 8.1 extensional-faulting event (e.g., Ammon et al., 2008; Lay et al., 2009). Historically, there was a large event on 1 May 1915 ($M_{W\text{-}ISCGEM}$ 7.8) in the central Kuril Islands (Fedotov et al., 1982) that may have ruptured the megathrust in the central region (Fig. 1), but details of that rupture are unknown and the interplate coupling between the 1952 and 2006 events remains uncertain.

3. Major near-trench intraplate compressional events

The 2020 Paramushir event is among the 5 largest recorded near-trench intraplate compressional events. This is an important category of tectonic events, so we compile the recorded occurrence and key seismic parameters of the largest of these events. Fig. 3 shows GCMT moment tensors or earlier mechanism solutions for all 24 such events with $M_W \geq 7.0$ from 1963 to 2020 (see source parameters in Table 1). Raessi and Atakan (2009) estimate M_W 7.65 for the 16 March 1963 central Kuril event (Fig. 1a; M_S 7.2) noted by Christensen and Ruff (1988). However, their slip model based on WWSSN recordings appears to have unreliable large shallow slip, so that magnitude is likely overestimated and we adopt the M_S value. The events included in Fig. 3 are selected based on mechanism, location, depth and size. Most events are confidently identified as intraplate compression near the trench. Two are ambiguous: the 8 December 2016 M_W 7.8 Solomon Islands event locates on the landward side of the trench and could possibly involve unusually steeply-dipping (50°) interplate thrusting (or overestimation of the dip), and the 12 April 2008 M_W 7.1 Macquarie event is at the northern end of the Hjort Trench and may represent along-strike growth of the evolving subduction zone.

The distribution of major near-trench compressional events is non-uniform, with no occurrences along many subduction zones.

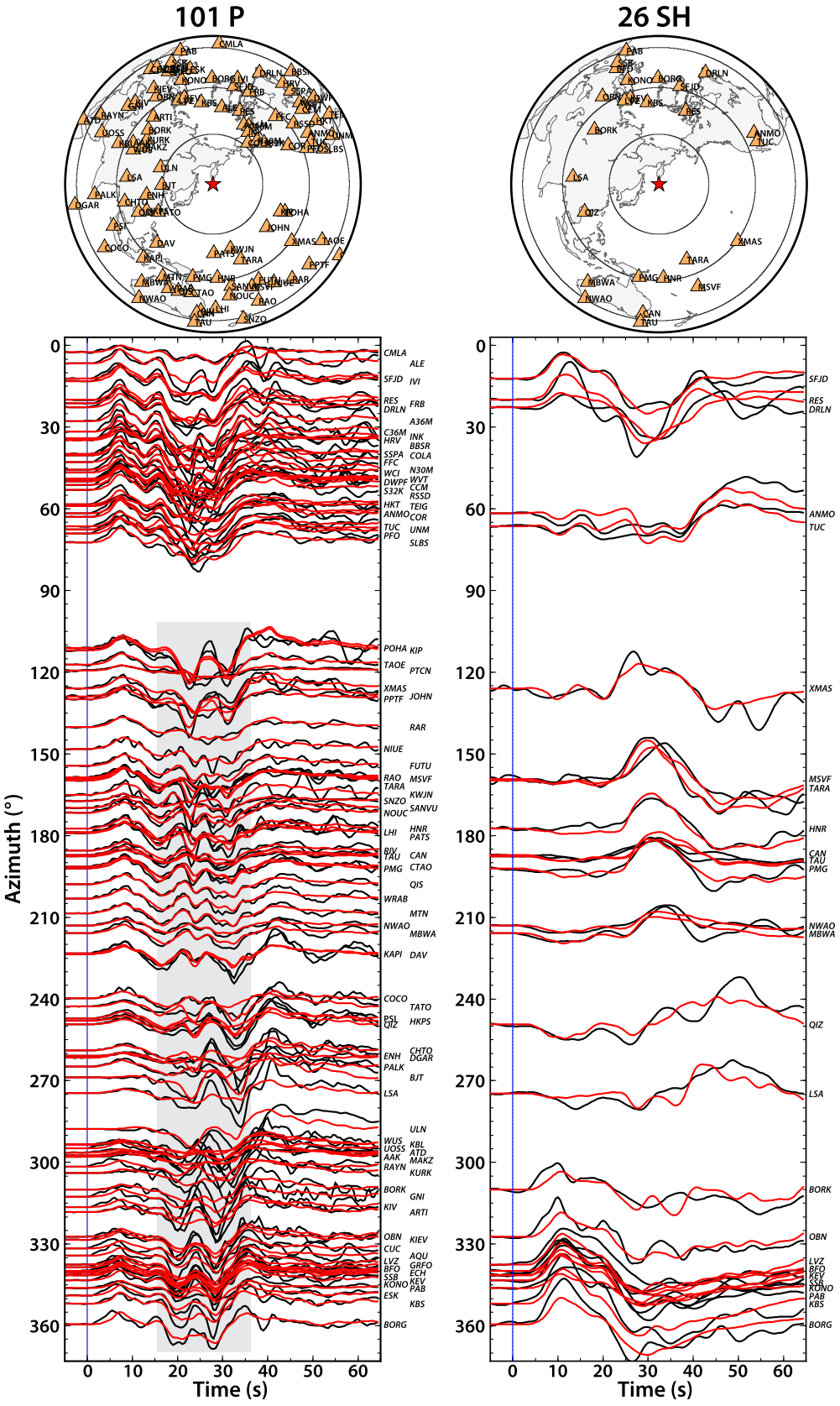

Fig. 2. The azimuthal and distance distribution of the P and SH wave recordings for the 2020 Paramushir M_W 7.5 earthquake with the observed (black lines) and model predictions (red lines) from the slip model on the northwest-dipping fault plane shown in Fig. 1. The gray rectangle box highlights the improved fitting on depth phases at stations to the west, compared to that from the inverted slip distribution from the southeast-dipping fault plane (Fig. S2).

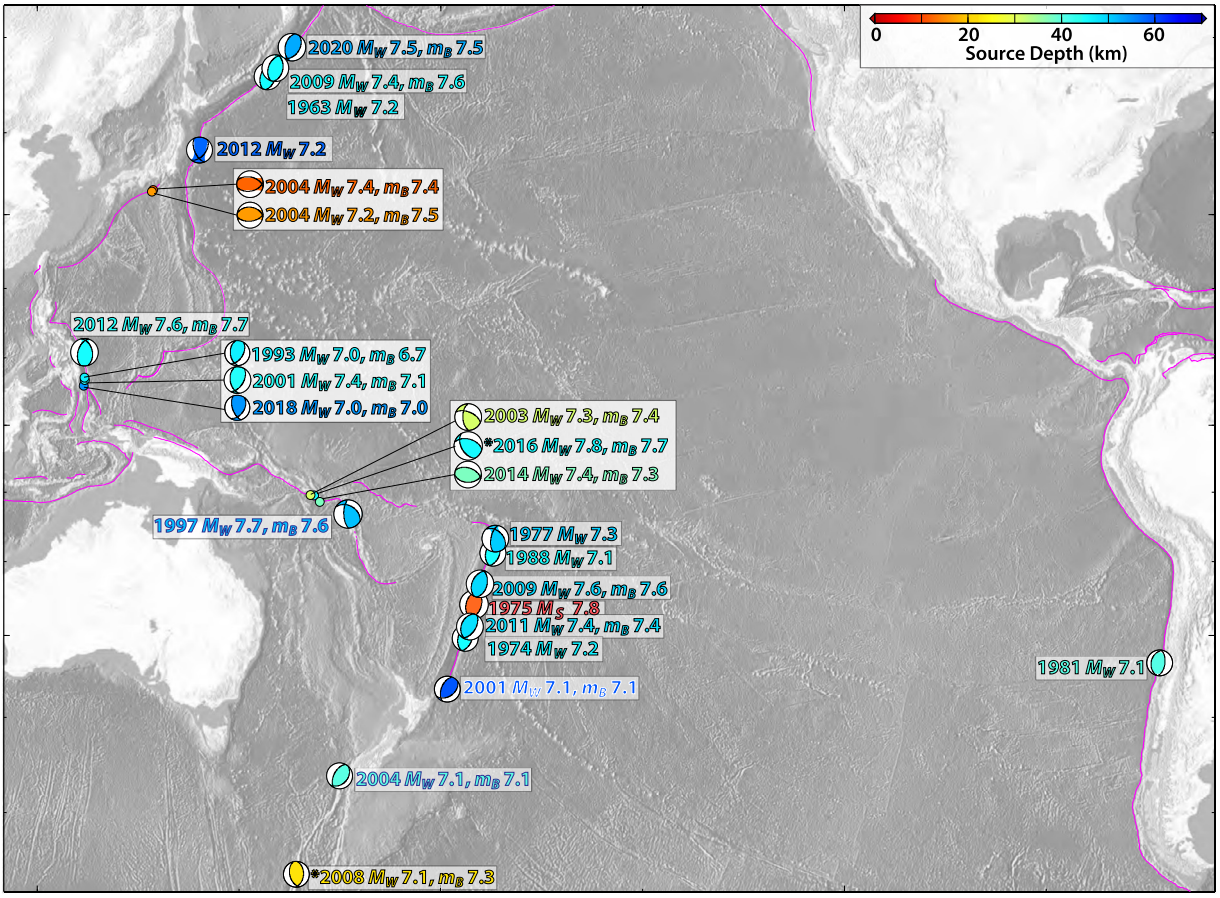

Fig. 3. Global distribution of major ($M_W \geq 7.0$) near-trench intraplate compressional earthquakes from 1963 to 2020. GCMT or other (pre-1976) focal mechanisms are shown, scaled in radius proportional to M_W and with compressional quadrants color-coded for centroid depth. The GCMT M_W is indicated along with m_B, computed for dominant periods of 3 to 5 s using the procedure of Kanamori and Ross (2020). Asterisks indicate two events for which classification as intraplate compression is ambiguous. The event parameters are listed in Table 1.

Most activity has been along the Kuril, Japan, Philippine, Solomon Islands, Tonga, Kermadec, and Chile zones. Several such events have preceded major interplate events in the Kuril, Tonga, Kermadec and Chile zones, as discussed below. The 2020 M_W 7.5 Paramushir and 2004 M_W 7.4 Nankai Trough events are located seaward of regions where great interplate events occurred more than 68 yrs ago, while some others are in regions of uncertain interplate coupling such as the eastern Philippines and northern Tonga. The Solomon Islands has many interplate and intraplate events, making it hard to establish any temporal patterns.

In addition to the M_W value for the events in Fig. 3, we show m_B measurements for ~3-5 s period P waves by the procedure of Ye et al. (2017) and Kanamori and Ross (2020) for events after 1990. For the 2020 Paramushir event, m_B is 7.53, slightly larger than M_W. Comparable relative values are found for the other near-trench compressional events. These measurements are compared with values for other intraplate events, interplate megathrust events at typical depths, and interplate tsunami earthquakes at shallow depths in Fig. 4a. The intraplate compressional events (red stars) as a group tend to have high m_B relative to M_W, similar to other intraplate events, indicating relatively large short-period seismic wave amplitudes. This tendency is also apparent in comparisons of moment-scaled radiated energy, E_R/M_0, as seen in Fig. 4b. We estimate the broadband radiated energy of the 2020 Paramushir event to be $E_R = 8.1 \times 10^{15}$ J following the procedure of Ye et al. (2016). This estimate is comparable to the broadband estimate provided by IRIS, $E_R = 7.6 \times 10^{15}$ J (http://ds.iris.edu/spud/eqenergy/18100564), based on the procedure of Convers and Newman (2011). The 2020 Paramushir event is typical of intraplate events in having higher value than interplate events. The location of intraplate compressional events within the central core of the oceanic lithosphere and the likelihood that the faulting is relatively infrequent may contribute to the high short-period energy typical of this class of event. The 3.5 MPa stress drop estimate for the 2020 event is also higher than the typical ~0.6 MPa stress drop for interplate thrust events (Ye et al., 2016). The stress drop and radiated energy measures indicate that the deep compressional environment in the bending slab readily supports elastic strain accumulation and brittle failure over a significant depth extent.

4. Discussion

4.1. Is there a general temporal pattern for the trench slope activity?

Regional interactions between fault systems are now broadly accepted as possible, and it is important to evaluate whether temporal patterns support a hypothesis of influence of interplate faulting cycles on intraplate activity near the trench. There have been a handful of reported cases of major near-trench intraplate compressional faulting events occurring prior to and seaward of large interplate ruptures: notably 1) the 16 October 1981 M_W 7.1 event (Fig. 3) before the 3 March 1985 Chile M_W 8.0 earthquake (e.g., Christensen and Ruff, 1983, 1988; Lay et al., 1989; Honda and Kawakatsu, 1990; Tichelaar et al., 1992); 2) the 2 July 1974 M_W 7.3 event before the 14 January 1976 Kermadec doublet (M_W 7.8, 7.9) (e.g., Christensen and Ruff, 1988; Lay et al., 1989; Todd and Lay, 2013); 3) the 11 October 1975 M_W 7.4 event before the 19 December 1982 M_W 7.5 Tonga event (e.g., Christensen and Ruff, 1988;

Table 1
Near-trench $M_W \geq 7.0$ intraplate compressional earthquakes from 1963 to 2020. Hypocentral parameters from NEIC.

Date	Origin Time (UTC)	Lat. (°)	Lon. (°)	Dep. (km)	M_W GCMT	M_0 GCMT (Nm)	Dep. GCMT (km)	m_B Median	E_R (J) E_R_B (J) E_R_FF (J)	E_R/M_0
16 Mar. 1963	08:44:50.0	46.64	154.78	15	7.2[#]	7.94×10^{19}[#]	-	-	-	-
2 July 1974	23:26:26.6	29.08	−175.95	33	7.2[£]	-	-	-	-	-
11 Oct. 1975	14:35:15.0	−24.89	−175.12	9	7.4[&]	-	-	-	-	-
2 Apr. 1977	07:15:22.7	−16.70	172.10	33.0	7.28	1.03×10^{20}	50.3	-	-	-
16 Oct. 1981	03:25:42.2	−33.13	−73.07	33.0	7.07	5.11×10^{19}	40.4	-	-	-
8 Oct. 1988	00:46:24.5	−18.77	−172.42	35.2	7.06	4.83×10^{19}	45.0	-	-	-
11 May 1993	18:26:48.2	7.23	126.62	33.0	6.95	3.36×10^{19}	46.5	6.67	3.82×10^{14} 6.43×10^{14}	1.1×10^{-5}
21 Apr. 1997	12:02:26.4	−12.58	166.68	33.0	7.69	4.39×10^{20}	51.2	7.63	2.46×10^{16} 1.29×10^{17}	5.6×10^{-5}
1 Jan. 2001	06:57:04.2	6.90	126.58	33.0	7.43	1.73×10^{20}	44.0	7.11	2.50×10^{15} 7.31×10^{15}	1.4×10^{-5}
21 Aug. 2001	06:52:06.2	−36.81	−179.57	33.0	7.08	5.16×10^{19}	59.0	7.12	4.77×10^{15} 7.73×10^{15}	9.2×10^{-5}
20 Jan. 2003	08:43:06.1	−10.49	160.77	33.0	7.25	9.34×10^{19}	31.0	7.43	8.17×10^{15} 4.29×10^{16}	8.7×10^{-5}
5 Sept. 2004	10:07:07.8	33.07	136.62	14.0	7.19	7.76×10^{19}	16.0	7.49	3.06×10^{15} 5.97×10^{16}	3.9×10^{-5}
5 Sept. 2004	14:57:18.6	33.18	137.07	10.0	7.37	1.45×10^{20}	12.0	7.44	4.25×10^{15} 4.53×10^{16}	2.9×10^{-5}
22 Nov. 2004	20:26:23.9	−46.60	164.72	10.0	7.10	5.57×10^{19}	40.0	7.10	1.10×10^{15} 6.92×10^{15}	2.0×10^{-5}
12 Apr. 2008[§]	00:30:12.6	−55.66	158.45	16.0	7.09	5.52×10^{19}	22.0	7.26	1.18×10^{15} 1.67×10^{16}	2.1×10^{-5}
15 Jan. 2009	17:49:39.1	46.86	155.15	36.0	7.38	1.50×10^{20}	45.2	7.57	5.26×10^{15} 9.29×10^{16} 5.27×10^{15}*	3.5×10^{-5}*
19 Mar. 2009	18:17:40.9	−23.05	−174.66	34.0	7.62	3.40×10^{20}	49.1	7.57	1.23×10^{16} 9.29×10^{16} 8.30×10^{15}*	2.4×10^{-5}*
21 Oct. 2011	17:57:16.1	−28.99	−176.24	33.0	7.38	1.48×10^{20}	48.4	7.36	3.04×10^{15} 2.91×10^{16}	2.1×10^{-5}
31 Aug. 2012	12:47:33.4	10.81	126.64	28.0	7.62	3.37×10^{20}	45.2	7.68	1.84×10^{16} 1.71×10^{17} 1.60×10^{16}*	4.7×10^{-5}*
7 Dec. 2012	08:18:24.3	37.89	144.09	36.1	7.20	7.89×10^{19}	57.8	7.56	6.14×10^{15} 8.79×10^{16}	7.8×10^{-5}
13 Apr. 2014	12:36:19.2	−11.46	162.05	39.0	7.44	1.79×10^{20}	37.5	7.29	3.02×10^{15} 1.98×10^{16}	1.7×10^{-5}
8 Dec. 2016[§]	17:38:46.3	−10.68	161.32	40.0	7.80	6.34×10^{20}	45.5	7.71	4.67×10^{16} 2.01×10^{17}	7.4×10^{-5}
29 Dec. 2018	03:39:09.7	5.90	126.92	60.2	6.98	3.72×10^{19}	54.4	7.00	- 3.98×10^{15}	-
25 Mar. 2020	02:49:32.4	49.00	157.69	56.7	7.48	2.09×10^{20}	52.9	7.53	7.60×10^{15} 7.45×10^{16} 5.97×10^{15}*	2.9×10^{-5}*

M_W, M_0, centroid depth from Global Centroid Moment Tensor (GCMT) catalog, unless [#]ISCGEM, [£]M_S or [&]Christensen and Lay (1988).
E_R from BB radiated P wave energy reported by IRIS (https://ds.iris.edu/spud/eqenergy), computed from m_B (second value), or computed using finite fault model and broadband data (*).
E_R/M_0 uses seismic moment from GCMT and E_R from BB radiated P wave energy unless value for finite-fault model is available (*).
§ Indicates that event designation as intraplate has uncertainty.

Christensen and Lay, 1988; Lay et al., 1989; Meng et al., 2015); and 4) the 16 March 1963 M_S 7.2 event before the 15 November 2006 central Kuril Islands M_W 8.3 earthquake (e.g., Lay et al., 2009; Raessi and Atakan, 2009). The 21 April 1997 M_W 7.7 rupture in northern Vanuatu (Fig. 3) occurred within the plate beneath large interplate M_W 7.7 and 7.9 ruptures on 7 October 2009 (e.g., Cleveland et al., 2014), so while it is further down-dip than most of the other events, it appears to be another instance of major compressional intraplate stress release prior to interplate rupture. There are multiple reported examples of smaller near-trench compressional events prior to large interplate earthquakes along Honshu, northern Vanuatu, and northern Chile (e.g., Christensen and Ruff, 1988; Craig et al., 2014), which appear to indicate temporal modulation of the compressional regime.

In contrast, major near-trench intraplate compressional faulting was not found to follow larger interplate ruptures in the compilation presented by Lay et al. (1989), supporting the hypothesis that reduction of interplate compressional strain during the mainshock ephemerally reduced the likelihood of subsequent large near-trench compressional activity. However, there are now two known cases, which are the 15 January 2009 M_W 7.4 event (Fig. 3) seaward of the 2006 Kuril Islands event (e.g., Lay et al., 2009), and the 7 December 2012 M_W 7.2 event (Fig. 3) seaward of the 11 March 2011 M_W 9.0 Tohoku earthquake (e.g., Lay et al., 2013; Kubota et al., 2012). Craig et al. (2014) infer that there is no temporal pattern to near-trench compressional faulting relative to interplate cycles based primarily on these two events occurring after adjacent underthrusting rupture. These events clearly indicate that compressional stress, presumably from slab bending, is not completely overwhelmed by the transient tensional stress increase following interplate faulting, but that is hardly surprising given that the slab remains bent. It is important to consider that both events had very extensive shallow tensional faulting sequences with much larger cumulative moment in close space/time proximity prior to

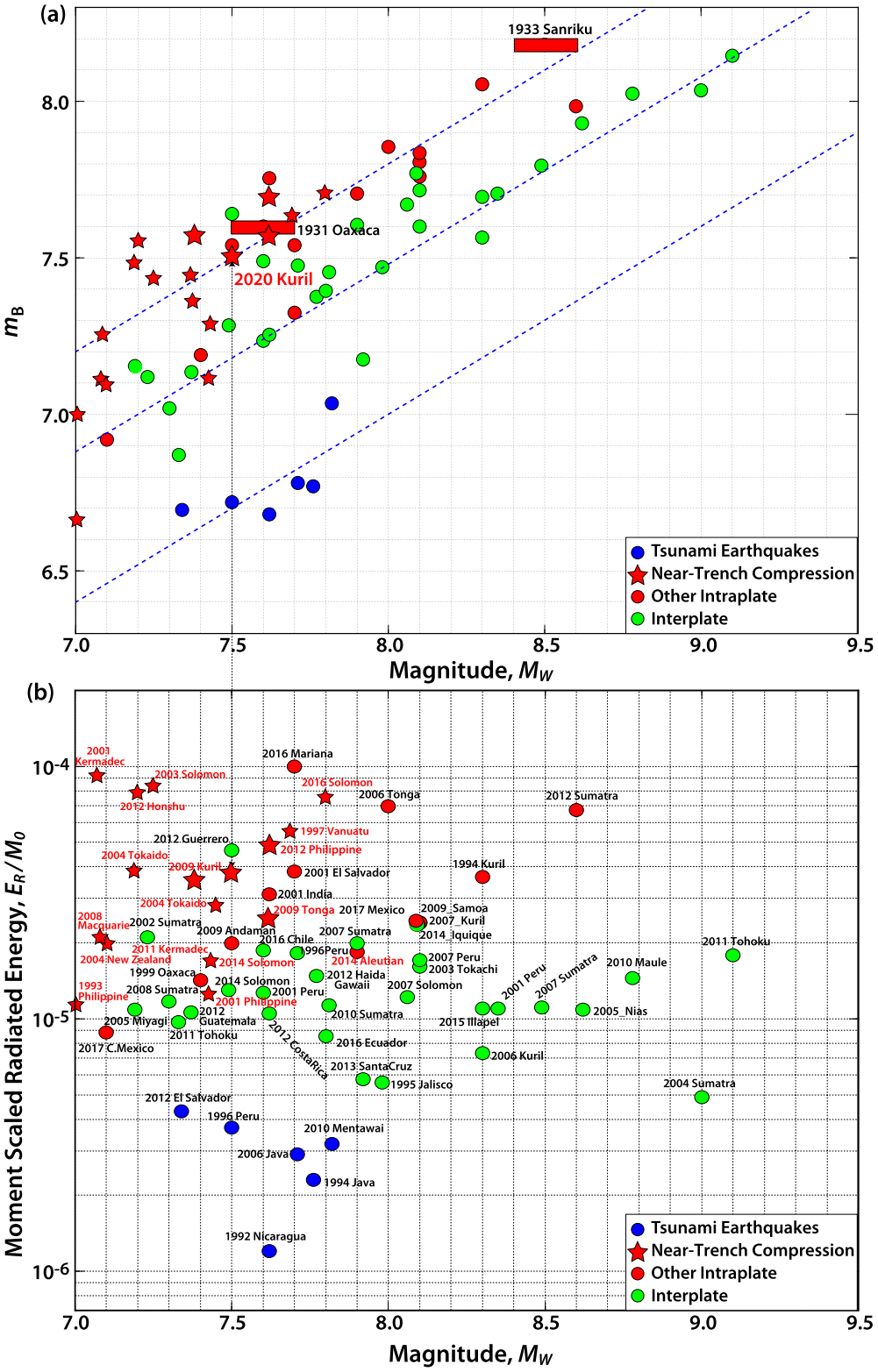

Fig. 4. Comparisons of (a) m_B for periods of ~3-5 s, with dashed blue lines indicating scaling curves for intraplate, interplate and tsunami earthquake (updated from Ye et al. (2017)), and (b) E_R/M_0 with M_W for different categories of earthquakes including shallow interplate tsunami earthquakes (blue), interplate thrusts (green), and intraplate (red) including near-trench intraplate compressional faulting (red stars). The early events labeled in the upper panel lack E_R measurements.

the compressional faulting, unlike the situation for isolated precursory compressional events discussed above including the 2020 Paramushir event, and there is almost no additional compressional activity in these two outlying sequences. Thus, inference that there is no influence of the intraplate stress cycle based on these events is questionable.

Many regions lacking large interplate events do have comparable-size compressional activity, so bending alone could plausibly account for major near-trench compressional failure with little or no role played by interplate faulting, but time-variation during the interplate seismic cycle can be considered for strongly coupled regions. The great 2009 M_W 8.1 Samoa normal-faulting earthquake

immediately preceded M_W 8.0 interplate thrust faulting (e.g., Beavan et al., 2010; Lay et al., 2010; Fan et al., 2016), but it appears that this involved along-strike dynamic triggering, so it seems to be a distinct phenomenon.

In order to evaluate whether the accumulated seismicity since the early studies of Christensen and Ruff (1988) and Lay et al. (1989) still provides support for the notion of temporal modulation of near-trench intraslab faulting by interplate strain accumulation and release, we consider the near-trench seismicity with $M \geq 5.0$ with known focal mechanisms before and after interplate thrust faults with $M \geq 8.0$ from 1920 to 1959 and with $M_W \geq 7.7$ from 1960 to 2020. We use the USGS-NEIC catalog to define the mainshocks and the seismicity sequences, with events with NEIC epicenters $\leq$40 km seaward of the trench and $\leq$10-20 km landward of the trench being considered. Focal mechanisms are obtained from the GCMT catalog from 1976 to 2020 and from the compilations of Christensen and Ruff (1988) and Lay et al. (1989) for events prior to 1975. The along-trench-strike search region is based on finite-fault solutions and/or aftershock areas for each mainshock. Re-rupture of a given segment with comparable size events occurs in several cases, and we subdivide the seismicity by the mid-point of the inter-event window.

The sequences of near-trench compressional and near-trench tensional activity for a total of 95 mainshocks (68 (71.5%) of which have at least some near-trench activity nearby) are displayed in Fig. 5, at vertical positions corresponding to the mainshock magnitude. The mainshocks contributing to this figure are located in all 16 subduction zones where $M_W \geq 7.7$ have occurred. Many zones have some mainshocks with relatively deep slip, which tends not to produce much near-trench activity (e.g., Wetzler et al., 2017; Sladen and Trevisan, 2018), so we focus on the collective behavior rather than subregion variations. This plot updates a similar display found in Lay et al. (1989), with more than an order of magnitude more events (611) being included. A gap in the relative time scale is provided to help separate activity before (red circles) and after (blue circles) the mainshock. There is intrinsically a greater observational period having small-event focal mechanism determinations after mainshocks than before, but most activity is distributed within $\pm$50 yrs of the mainshocks. Given the large number of major and great earthquakes that have occurred after 2000, there is good sampling of both before- and after-mainshock populations. If there is no influence of the mainshock stress cycle on the intraslab activity one would expect uniform distributions with time for both compressional and tensional activity.

The temporal effect of the mainshock on near-trench tensional activity is clearly evident, with 12 times more events (480/40) involving a factor of 5.9 higher cumulative seismic moment occurring in the full intervals after than before the mainshocks (Fig. 5b). Increased tensional activity is particularly concentrated in the first two decades after the mainshock, but can persist for many decades. In contrast to the data set shown by Lay et al. (1989), there are more examples of tensional events prior to large megathrust events, although none occur in the year or two immediately preceding the mainshocks. The overall distribution is what is expected for superposition of temporally-modulated shallow extensional stress from the interplate seismic cycle on an ambient shallow bending tensional stress regime. The temporal pattern for tensional activity is clearly manifested because the long interseismic interval will tend to suppress tensional activity with the abrupt interplate strain release concentrating activity and giving a clear signature.

Evaluating the compressional event activity (Fig. 5a) in this context, it is clear that there is a complementary pattern within a $\pm$25-yr time interval of 1.5 time more (37/24) with a factor of 1.3 higher cumulative moment for compressional events before than after the mainshock. The largest exceptions to this more subtle

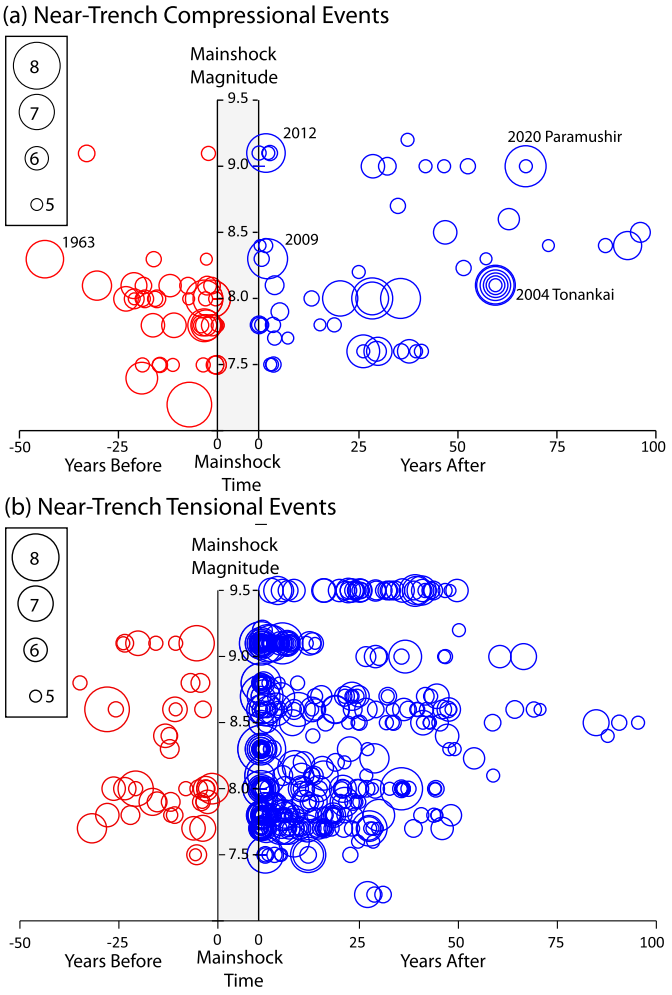

Fig. 5. Temporal patterns of a) near-trench compressional (~trench-normal P axis) intraslab events and b) near-trench extensional (~trench-normal T axis) intraslab events relative to occurrence time of mainshocks from 1920 to 2020. Each sequence is plotted along the corresponding mainshock magnitude on the vertical axes with circles scaled proportional to magnitude (inset legend) of the intraslab compressional/extensional event. Mainshocks involving interplate thrust faulting with $M_W \geq 8.0$ from 1920 to 1959 and with $M_W \geq 7.7$ from 1960 to 2020 are included, along with a couple of smaller mainshock events included by Lay et al. (1989). Red color highlights events prior to each mainshock and blue highlights events after each mainshock. The gray time intervals correspond to an artificial discontinuity in the time axis at the time of the mainshock to separate prior- and post-mainshock activity. Several large compressional events discussed in the text are labeled in a).

tendency are the two large events off Honshu in 2012 and off the Kuril Islands in 2009 discussed above, both of which occurred following and during high tensional event activity. About ~20 yrs after the mainshocks, there is steady increase in large compressional event activity, and the time frame from 20 to 100 yrs after the mainshock has a cumulative seismic moment for compressional events approximately twice that of tensional events. This may correspond to compressional stress build-up accompanying strain accumulation on the megathrust. The pattern is certainly less bimodal than for the sparser data set in the early compilation of Lay et al. (1989), but it seems reasonable to interpret the patterns as superposition of time-varying stress fields on a time-invariant background stress for both compressional and tensional activity. The temporal pattern for compressional activity is intrinsically less dramatic as the activity is expected to increase over extended time in the interseismic interval, with reduction in compressional stress after the mainshock giving a less clear decrease in activity than the increase for tensional events.

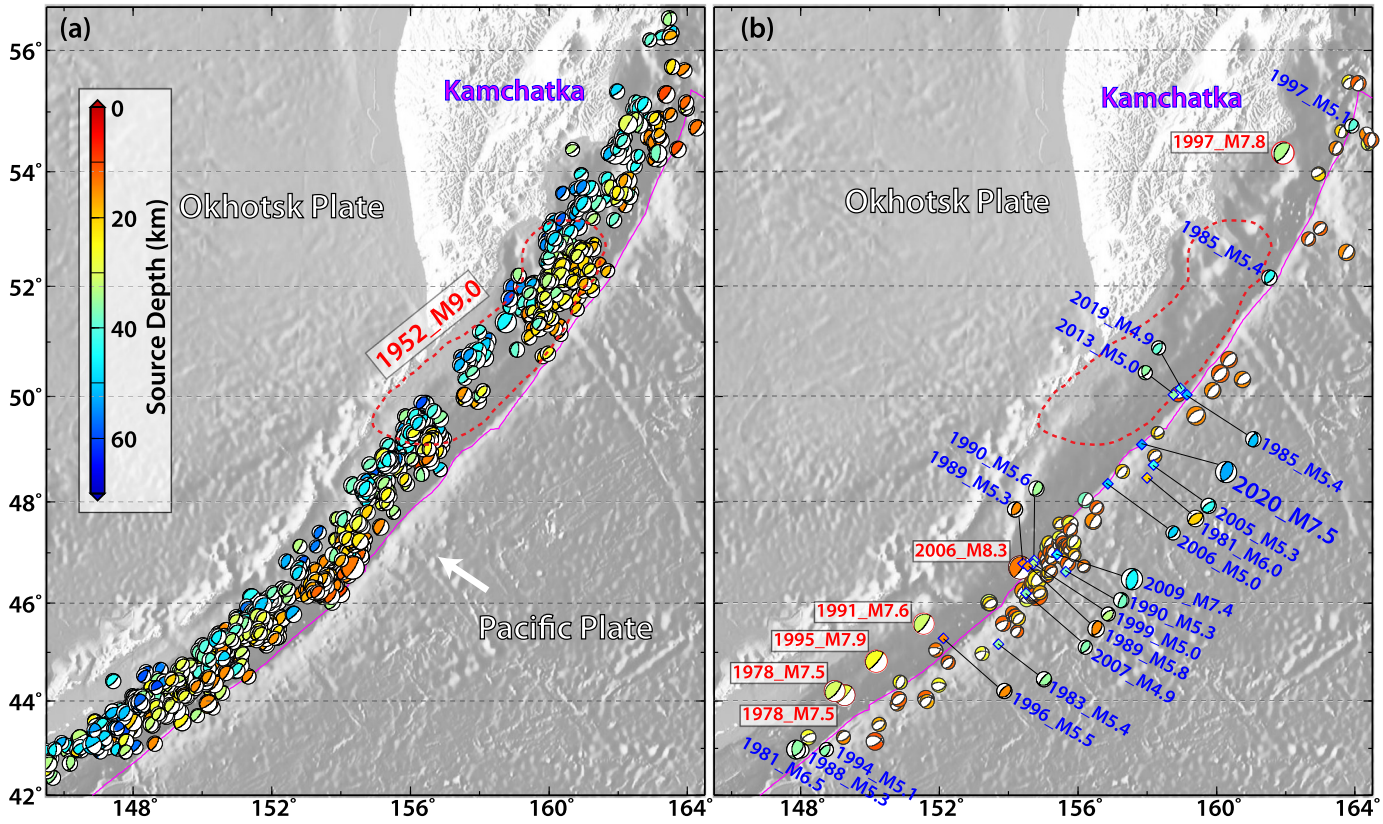

Fig. 6. Selected GCMT mechanisms from 1976-2020 for the subduction zone along the central and northern Kuril Islands and Kamchatka. Interplate thrust faulting events are shown in (a). Near-trench intraplate normal (not labeledas) and compressional faulting (blue labels) and large interplate thrust faulting events (red labels) are shown in (b). The red dashed curve in both (a) and (b) indicates the aftershock region of the 1952 M_W 9.0 Kamchatka earthquake (MacInnes et al., 2010). The moment tensors are color-coded by centroid depth and scaled relative to M_W.

The very largest mainshocks, such as 1960 Chile, 2004 Sumatra, 2010 Maule, 2011 Tohoku, all associated with rather shallow-dipping wide fault planes with modest outer-rise bending, do not have many prior compressional (or tensional) events. In these regions, the compressive stress caused by interplate coupling, combined with the modest bending compressive stress, may not be large enough to cause near-trench compressive activity. Thus, near-trench compressional activity is not always a robust indicator of interplate strain accumulation. The near-trench compressional activity may be influenced by other factors. For example, Tonga has numerous large compressional events, even along regions lacking a history of large interplate events, so the background activity from bending may be heightened in regions with strong plate bending (e.g., Craig et al., 2014). When large compressional events occur, their upper depth extent is important to consider, but this is usually very difficult to determine and has been controversial for events such as the 1981 Chile earthquake (e.g., Ward, 1983; Christensen and Ruff, 1985; Honda and Kawakatsu, 1990; Tichelaar et al., 1992; Tilmann et al., 2008; Craig et al., 2014). Occurrence of megathrust events produces short time-scale perturbations and temporal patterns are intrinsically more evident, particularly for the shallow extensional regime, as in Fig. 5b. Compressional stress accumulation is a long-term process, with 100- to 1000-yr time scale, making it intrinsically difficult to observe temporal variation relative to a background level over intervals of 50-60 yrs. It is likely that given the range of magnitude of strain accumulation for future great events spanned by our data set, any temporal variation in compressional stress may show up in the catalog as apparent spatial variation. Longer term observations are needed to fully quantify the role of temporal variations.

4.2. Implications of temporal patterns for the 2020 event

The framework developed by Christensen and Ruff (1983, 1988) and the global temporal patterns displayed in Fig. 5 suggest that occurrence of the 2020 M_W 7.5 Paramushir near-trench intraplate compressional earthquake, rupturing from ~30 to ~70 km deep into the Pacific plate seaward of a region of large interplate slip in the great 1952 Kamchatka earthquake, may be an indication of significant shear-stress build-up on the megathrust being superimposed on background plate bending stresses in the region. The relatively large depth extent of the 2020 rupture and the relatively strong radiated energy for the event suggest the presence of a broad elastic compressional stress regime below an elevated neutral surface in the plate, as expected for shear-stress accumulation on the plate boundary 68 yrs after the 1952 event. While no specific timing of future rupture of the interplate locked zone can be given based on Fig. 5, the unusually large seismic moment of the 2020 event focuses concern on the region given that several prior documented examples of similarly isolated, comparable size events have occurred late in the interplate seismic cycle, a few years to several decades ahead of adjacent megathrust ruptures (Fig. 5a).

Given that major near-trench events are rare, it is instructive to consider smaller near-trench earthquake activity along the northern Kuril Islands arc. Fig. 6 shows all GCMT moment tensors from 1976 to 2020 identified as probable interplate thrusting (Fig. 6a) or near-trench extensional and compressional faulting (Fig. 6b). The interplate thrust events larger than M_W 7.5 are included in Fig. 6b for reference. Interplate activity just southwest of the Kamchatka peninsula is relatively sparse; this area corresponds to where MacInnes et al. (2010) infer large slip in 1952. The 2020 event occurred near the southwestern end of this region. A mix of smaller tensional and compressional activity with magni-

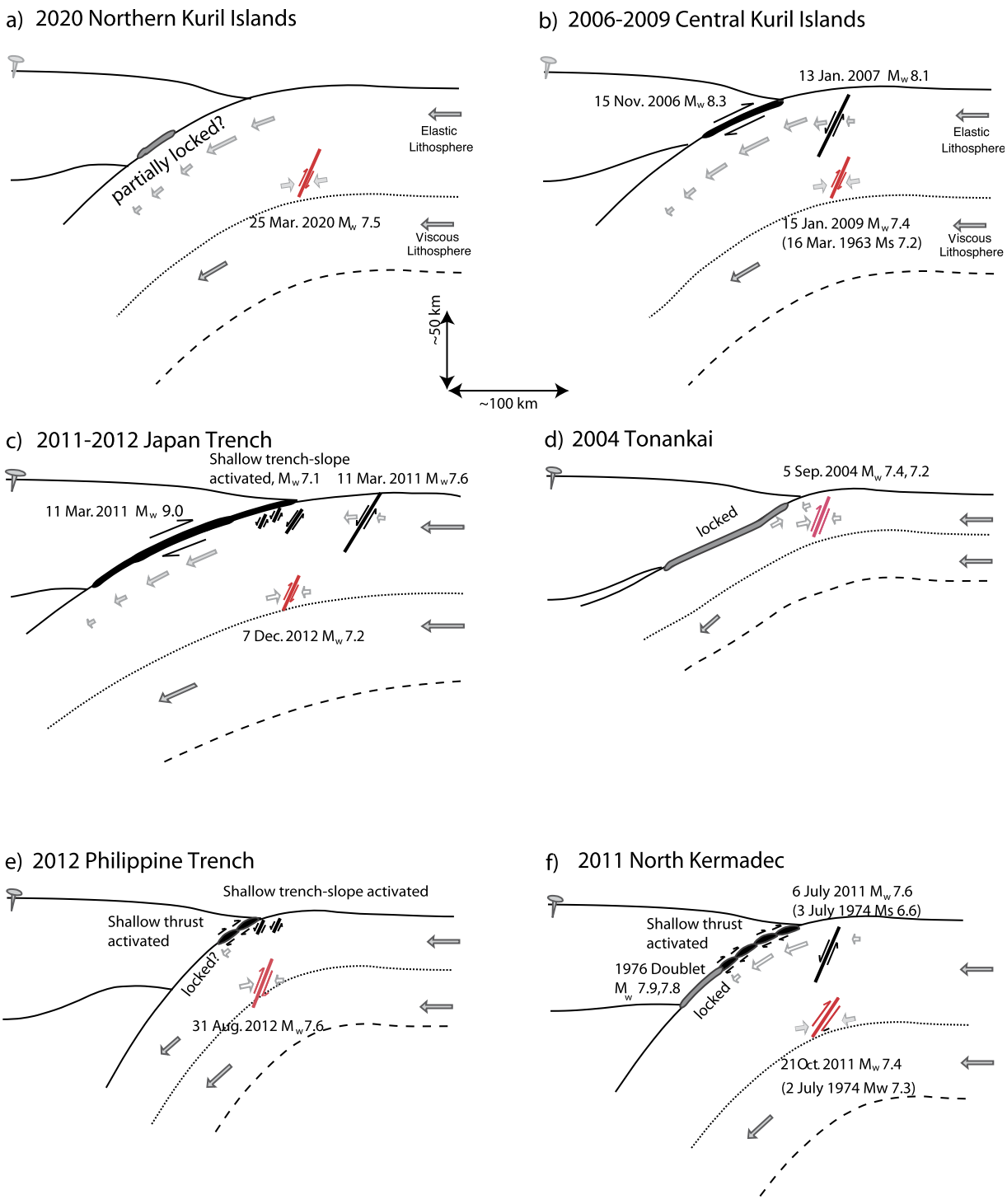

Fig. 7. Schematic cross-sections for several western Pacific subduction zones that have hosted major near-trench intraplate compressional faulting (highlighted in red). The cross-sections are roughly scaled to be appropriate for each region. a) The partially locked northern Kuril subduction zone hosting the 25 March 2020 M_W 7.5 event. b) The shallowly coupled central Kuril Islands subduction zone that had a compressional event in 1963, a great interplate event in 2006 and shallow normal and deeper thrusting intraplate events in 2007 and 2009, respectively. c) The Japan trench region offshore of Honshu struck by the great 2011 Tohoku thrust event and subsequent numerous extensional events and the deep compressional event of 2012. d) The Nankai trench region along the great 1944 Tonankai interplate rupture, which is locked and had shallow compressional events in 2004. e) The central Philippine trench with uncertain coupling which had a 2012 compressional event that triggered shallow interplate thrusting and intraplate extensional activity. f) The northern Kermadec region where a large compressional event in 1974 preceded interplate thrusts in 1976, followed by large shallow intraplate extension and deep intraplate compression in 2011.

tudes <6.0 is located along the trench on either side of the 2020 event, indicative of background bending stresses. There is not a clear indication that this region had significantly more near-trench seismicity following the 1952 event, but there is little constraint on the up-dip limit of slip in 1952. If slip in that event did not extend to the trench there may not have been a corresponding increase in intraplate faulting (e.g., Wetzler et al., 2017; Sladen and Trevisan, 2018).

Fig. 7a provides a sketch cross-section near the 2020 Paramushir event. For this region, the interplate megathrust appears to have had large slip in 1952 and is at least partially locked. About 5 m of slip deficit could have accumulated since 1952. The large 25

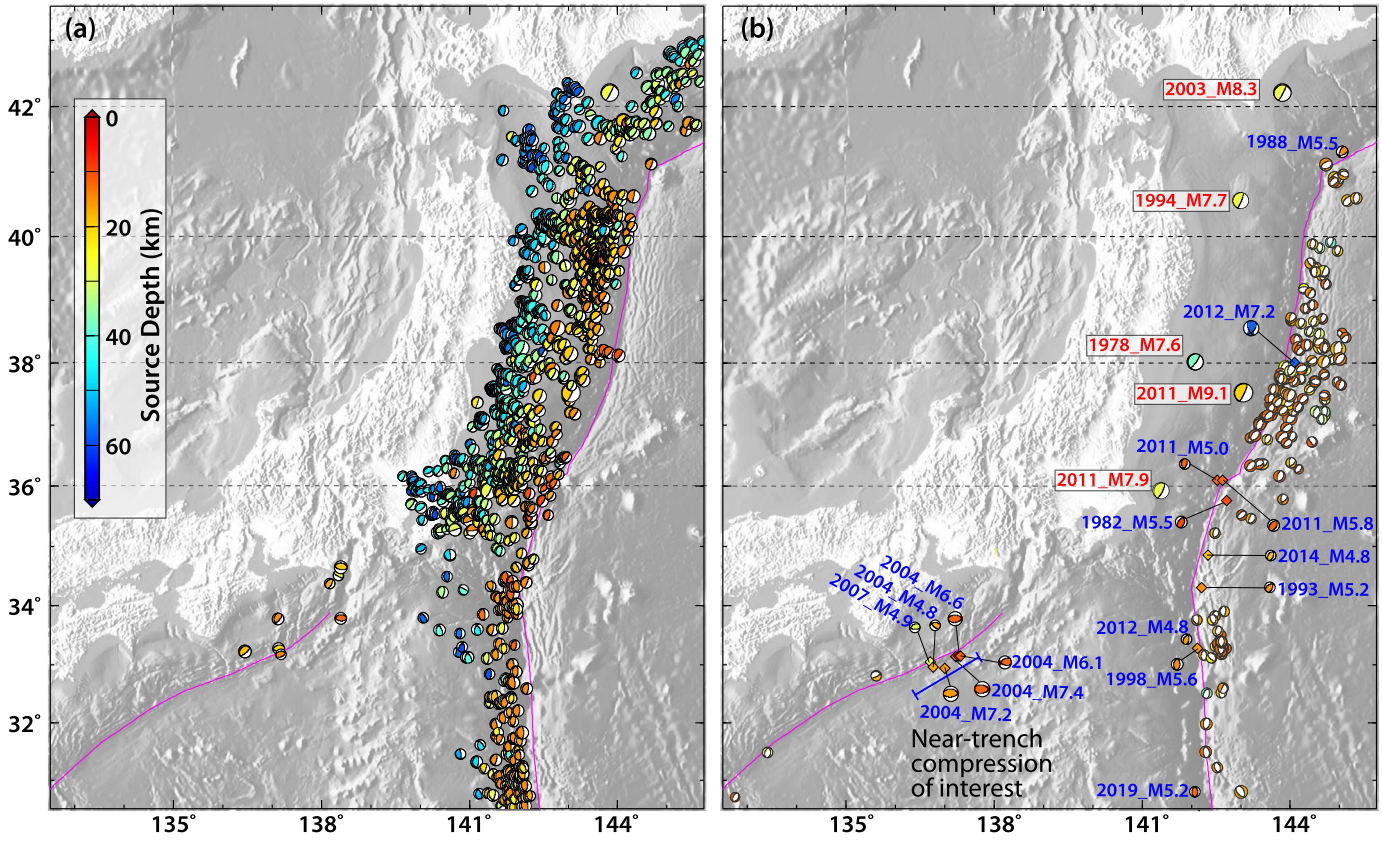

Fig. 8. Selected GCMT mechanisms from 1976-2020 for the subduction zones along Japan. Interplate thrust faulting events are shown in (a). Near-trench normal faulting (not labeled), compressional intraplate faulting (blue labels), and large interplate thrust events (red labels) are shown in (b). The moment tensors are color-coded by centroid depth and scaled relative to M_W. A region of shallow near-trench compressional faulting seaward of the 1944 Tonankai earthquake along the Nankai trench is highlighted. This activity is discussed in the text.

March 2020 event 68 yrs after the great event locates seaward of this zone in a region with additional much smaller compressional and tensional events near the trench (Fig. 6).

4.3. Implications of temporal patterns for other large compressional events

Fig. 7 provides additional cross-sections for some of the other major near-trench compressional earthquakes in Fig. 3 to help visualize the diverse temporal patterns involved. Our focus is on how the intraplate activity varies relative to the large interplate thrust event in each sequence, to test the hypothesis that the interplate seismic cycle influences timing of the intraplate activity. If this is the case, large outer rise compressional activity seaward of mature locked interplate regions can provide a long-term gauge of stress accumulation on the megathrust. It does not provide a short-term precursor capability.

The central Kuril zone along the 2006 M_W 8.3 event is shown in Fig. 7b. This region had the major 1963 compressional event, likely smaller than the 2020 Paramushir event, followed by the great 2006 interplate thrusting and 2007 shallow extensional events and the subsequent 2009 deep compressional event. Lower magnitude events in this region are shown in Fig. 6b with six compressional events with magnitudes 5.0 to 5.8 having preceded the 2006 rupture and one M 4.9 event after the megathrust rupture. It is difficult to compare this sequence with the 2020 Paramushir region since the latter is far further into the interseismic cycle.

The sequence along the 2011 Tohoku rupture is shown in Fig. 7c, with the great interplate thrust activating extensive trench slope extensional faulting with M_W as large as 7.6. The 2012 near-trench doublet followed, with the deep compressional event and shallow extensional event within seconds of each other. The regional interplate thrusting activity is shown in Fig. 8a. Fig. 8b demonstrates a lack of compressional activity along the 2011 rupture prior to the rupture with several small compressional events to the south, before and after the M_W 7.9 megathrust aftershock on 11 March 2011.

Large compressional events in 2004 seaward of the 1944 Tonankai rupture zone are depicted in Fig. 7d and smaller events are highlighted in map view in Fig. 8b. This compressional activity is shallower than in other regions, extending to only about 25 km deep. This sequence has been intensively studied (e.g., Baba et al., 2005; Hara, 2005; Bai et al., 2007; Satake et al., 2005; Seno, 2005; Craig et al., 2014), mostly emphasizing static stress state rather than any temporal variation. Seno (2005) attributes the intraplate compressional stress to the along-strike collision of the Izu Peninsula with central Honshu, arguing that slab pull and ridge push will not be strong for the young Philippine Sea plate, and that rotation of the slab bending stress is required to predict the observed compression axes. The possible lack of strong slab pull may account for the absence of shallow extensional activity in this region, and one would also not expect large compressional activity if the bending effect is weak. However, the plate interface is known to be locked down-dip of the trench-slope activity, so temporal variation of the interplate locking could account for the compressional stress locating at shallow depth. The distance to the Izu collision is more than 100 km along strike, so it is unclear that collisional stress extends that far. The lack of other large near-trench compressional activity closer to the Izu collision zone is difficult to reconcile with it controlling the plate stress state as far away as the 2004 sequence.

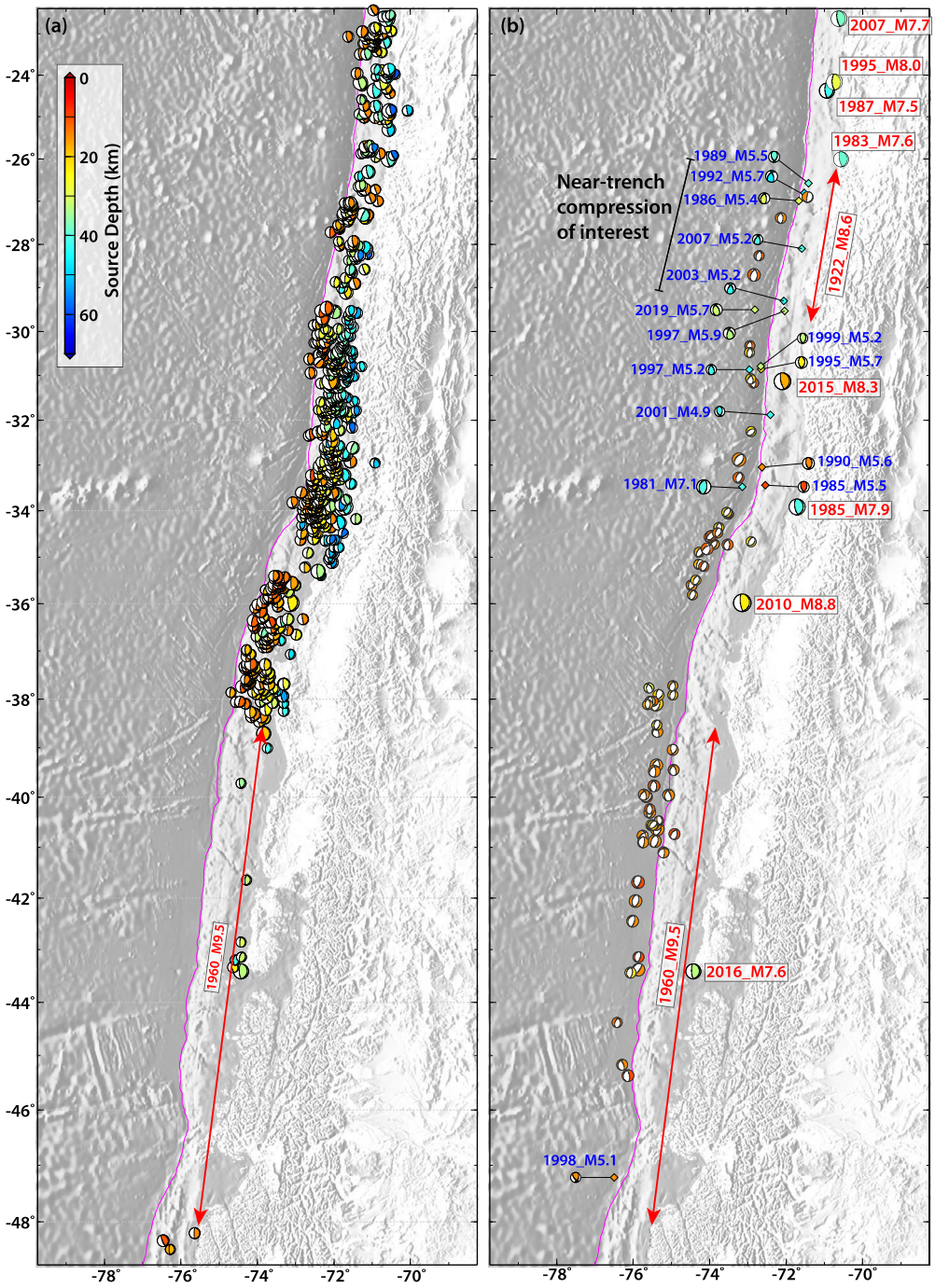

Fig. 9. GCMT mechanisms from 1976-2020 for the subduction zone along Chile. Interplate thrust faulting events are shown in (a). Near-trench normal faulting (not labeled), compressional intraplate faulting (blue labels), and large interplate thrust events (red labels) are shown in (b). The moment tensors are color-coded by centroid depth and scaled relative to M_W. A region of near-trench compressional activity is highlighted (black line) along the rupture zone of the 1922 Atacama M_W 8.6 event (red line with arrowheads).

The 2012 M_W 7.6 compressional event below the Philippine trench triggered shallow thrust faulting on the megathrust as well as shallow extensional faulting along the trench slope (Ye et al., 2012; Fig. 7e). Whether the deeper plate boundary is locked is not known, and there is no record of nearby large historical events. There is a mix of smaller extensional and compressional events along Mindanao (Fig. S4). Major compressional events along Mindanao (Fig. 3) are located near large historical events such as the 14 April 1924 M_W 8.2 event (e.g., Ye et al., 2012), but the degree of interplate coupling is uncertain.

The North Kermadec region where the 1976 M_W 7.9 and 7.8 interplate doublet occurred is shown in Fig. 7f. The doublet was preceded by near-trench compression in 1974, with a smaller near-trench extensional event. On 6 July 2011, a shallow near-trench tensional event occurred, triggering shallow interplate thrusting followed a few months later by the 21 October 2011 deeper compressional event (Fig. 3). GPS indicates that this region is locked at depth, but the record of large events prior to 1976 is limited. There has been up to 44 yrs of strain accumulation since the last large megathrust strain release. The occurrence of smaller outer rise compressional events intermixed with tensional events since

1976 is relatively high along the Tonga-Kermadec zone (Fig. S5). This includes activity in northern Tonga seaward of and prior to the 2009 triggered megathrust rupture ($M_W \sim 8.0$) following the Samoa earthquake. The uncertain nature of coupling and strain accumulation along the arc in other regions makes it difficult to argue for shear-stress accumulation on the megathrust influencing the outer rise activity, as the background activity from bending appears to be relatively high.

While there has not been a major near trench-slope compressional event along central and southern Chile since the 1981 event seaward of the 1985 interplate rupture, smaller ($\leq M_W$ 5.7) compressional activity did occur seaward prior to the 2015 M_W 8.3 Illapel rupture, and there have been six $M_W \leq 5.9$ compressional events along the 1922 Atacama M_W 8.6 megathrust rupture zone (highlighted in Fig. 9). This region is considered to be a mature seismic gap. While tensional activity is more common along the Chile trench, the localized regions with compressional activity do appear to be spatially related to great interplate rupture zones. The same is true for northern Chile and southern Peru (Fig. S6).

5. Conclusions

The major 25 March 2020 Paramushir near-trench intraplate compressional earthquake raises the question of whether accumulating megathrust slip-deficit in the southwestern portion of the great 1952 Kamchatka earthquake is enhancing intraplate compressional stress relative to that associated with bending of the lithosphere. We address this question by compiling the historical record of very large interplate ruptures and near-trench intraplate faulting. Variability in intraplate faulting patterns is partially due to up-dip extent of megathrust ruptures and varying slab curvature and associated bending stresses, but some temporal patterns are observed. Several regions where isolated large compressional events similar to the 2020 Paramushir rupture have occurred eventually experienced major interplate thrusting. Two examples of comparably large compressional events have occurred following great interplate ruptures (2009 Kuril, $M_W = 7.4$ and 2012 Sanriku, $M_W = 7.2$), but both occurred soon after the mainshocks following extensive shallow near-trench extensional faulting sequences with much larger cumulative moment. Given that near-trench extensional faulting clearly exhibits temporal modulation by large interplate ruptures, it is sensible that compressional faulting does as well, with the 2020 Paramushir event occurring 68 yrs into the interseismic strain accumulation interval. Deep intraplate compressional events as a group tend to have relatively high radiated energy indicative of extensive brittle material within the elastic compressional regime, supporting the possibility of temporal modulation by interplate ruptures. More GPS measurements along the northern Kuril Islands could determine the accumulating slip-deficit distribution. The occurrence of compressional slab activity seaward of the historic rupture zones along Tonankai, Japan, and Atacama, Chile, underscores the importance of establishing a better understanding of the connection between the trench slope stress state and the occurrence of megathrust earthquakes.

CRediT authorship contribution statement

LY performed the finite-fault inversion for the 2020 event. HK performed the W-phase inversion. TL performed the time-dependent analysis of near-trench sequences. LY, TL and HK conceived the project, jointly interpreted the result and wrote the manuscript collaboratively.

Declaration of competing interest

The authors declare that they have no known competing financial interests or personal relationships that could have appeared to influence the work reported in this paper.

Acknowledgements

Teleseismic waveforms were downloaded from the Incorporated Research Institutions for Seismology (IRIS) data management center (http://ds.iris.edu/wilber3/find_event). Global Centroid Moment Tensor Solutions are from https://www.globalcmt.org/CMTsearch.html. We use the earthquake catalog from National Earthquake Information Center at U.S. Geological Survey (USGS-NEIC) (https://earthquake.usgs.gov/earthquakes/). We thank Nadav Wetzler and an anonymous reviewer for their constructive reviews of the original manuscript. Lingling Ye's earthquake study is supported by National Natural Science Foundation of China (No. 41874056) and Fundamental Research Funds for the Central Universities, Sun Yat-sen University (No. 19lgzd11). Thorne Lay's earthquake research is supported by the U.S. National Science Foundation (Grant EAR1802364).

Appendix A. Supplementary material

Supplementary material related to this article can be found online at https://doi.org/10.1016/j.epsl.2020.116728.

References

Ammon, C.J., Kanamori, H., Lay, T., 2008. A great earthquake doublet and seismic stress transfer cycle in the central Kuril islands. Nature 451, 561–565. https://doi.org/10.1038/nature06521.

Baba, T., Cummins, P.R., Hori, T., 2005. Compound fault rupture during the 2004 off the Kii Peninsula earthquake (M 7.4) inferred from highly resolved coseismic sea-surface deformation. Earth Planets Space 57, 167–172.

Bai, L., Bergman, E.A., Engdahl, E.R., Kawasaki, I., 2007. The 2004 earthquake offshore of the Kii peninsula, Japan: hypocentral relocation, source process and tectonic implications. Phys. Earth Planet. Inter. 165, 47–55.

Beavan, J., Wang, X., Holden, C., Wilson, K., Power, W., Prasetya, G., Bevis, M., Kautoke, R., 2010. Near-simultaneous great earthquakes at Tongan megathrust and outer rise in September 2009. Nature 466, 959–963.

Bürgmann, R., Kogan, M.G., Steblov, G.M., Hilley, G., Levin, V.E., Apel, E., 2005. Interseismic coupling and asperity distribution along the Kamchatka subduction zone. J. Geophys. Res. 110, B07405. https://doi.org/10.1029/2005JB003648.

Chapple, W.M., Forsyth, D.W., 1979. Earthquakes and bending of plates at trenches. J. Geophys. Res. 84, 6729–6749.

Christensen, D.H., Lay, T., 1988. Large earthquakes in the Tonga region associated with subduction of the Louisville Ridge. J. Geophys. Res. 93, 13,367–13,389.

Christensen, D.H., Ruff, L.J., 1983. Outer-rise earthquake and seismic coupling. Geophys. Res. Lett. 10, 697–700.

Christensen, D.H., Ruff, L.J., 1985. Analysis of the trade-off between hypocentral depth and source time function. Bull. Seismol. Soc. Am. 75, 1637–1656.

Christensen, D.H., Ruff, L.J., 1988. Seismic coupling and outer rise earthquakes. J. Geophys. Res. 93 (B11), 13,421–13,444.

Cleveland, K.M., Ammon, C.J., Lay, T., 2014. Large earthquake processes in the northern Vanuatu subduction zone. J. Geophys. Res., Solid Earth 19, 8866–8883. https://doi.org/10.1002/2014JB011289.

Convers, J.A., Newman, A.V., 2011. Global evaluation of large earthquake energy from 1997 through mid-2010. J. Geophys. Res. 116, B08304. https://doi.org/10.1029/2010JB007928.

Craig, T.J., Copley, A., Jackson, J., 2014. A reassessment of outer-rise seismicity and its implications for the mechanics of oceanic lithosphere. Geophys. J. Int. 197, 63–89. https://doi.org/10.1093/gji/ggu013.

Dmowska, R., Rice, J.R., Lovison, L.C., Josell, D., 1988. Stress transfer and seismic phenomena in coupled subduction zones during the earthquake cycle. J. Geophys. Res. 93 (B7), 7869–7884. https://doi.org/10.1029/JB093iB07p07869.

Fan, W., Shearer, P.M., Ji, C., Bassett, D., 2016. Multiple branching rupture of the 2009 Tonga-Samoa earthquake. J. Geophys. Res. 121, 5809–5827. https://doi.org/10.1002/2016JB012945.

Fedotov, S.A., Chernyshev, S.D., Chernysheva, G.V., 1982. The improved determination of the source boundaries for earthquakes of M > 7.75, of the properties of the seismic cycle, and of long-term seismic prediction for the Kurile-Kamchatka arc. EPR, Earthqu. Predict. Res. 1, 153–171.

Gusev, A.A., 2006. Large earthquakes in Kamchatka: locations of epicentral zones for the instrumental period. J. Volcanol. Seismol. 6, 39–42 (in Russian with English abstract).

Hara, T., 2005. Change of the source mechanism of the mainshock of the 2004 off the Kii Peninsula earthquakes inferred from long period body wave data. Earth Planets Space 57, 179–183.

Hartzell, S.H., Heaton, T.H., 1983. Inversion of strong ground motion and teleseismic waveform data for the fault rupture history of the 1979 Imperial Valley, California, earthquake. Bull. Seismol. Soc. Am. 73 (6A), 1553–1583.

Honda, S., Kawakatsu, H., 1990. The depth of the October 1981 off Chile outer-rise earthquake ($M_S = 7.2$) estimated by a comparison of several waveform inversion methods. Bull. Seismol. Soc. Am. 80, 69–87.

Johnson, J.M., Satake, K., 1999. Asperity distribution of the 1952 great Kamchatka earthquake and its relation to future earthquake potential in Kamchatka. Pure Appl. Geophys. 154, 541–553.

Kanamori, H., Rivera, L., 2008. Source inversion of W phase: speeding up seismic tsunami warning. Geophys. J. Int. 175, 222–238. https://doi.org/10.1111/j.1365-246X.2008.03887.x.

Kanamori, H., Ross, Z.E., 2020. Reviving m_B. Geophys. J. Int. 216, 1798–1816. https://doi.org/10.1093/gji/ggy510.

Kelleher, J., Savino, J., 1975. Distribution of seismicity before large strike-slip and thrust-type earthquakes. J. Geophys. Res. 80, 260–271.

Kelleher, J., Sykes, L., Oliver, J., 1973. Possible criteria for predicting earthquake locations and their application to major plate boundaries in the Pacific and the Caribbean. J. Geophys. Res. 78, 2547–2585.

Kikuchi, M., Kanamori, H., 1991. Inversion of complex body waves—III. Bull. Seismol. Soc. Am. 81 (6), 2335–2350.

Kubota, T., Hino, R., Inazu, D., Suzuki, S., 2012. Fault model of the 2012 doublet earthquake, near the up-dip end of the 2011 Tohoku-Oki earthquake, based on a near-field tsunami: implications for intraplate stress state. Prog. Earth Planet. Sci. 6, 67. https://doi.org/10.1186/240645-019-0313-y.

Lay, T., Astiz, L., Kanamori, H., Christensen, D.H., 1989. Temporal variation of large intraplate earthquakes in coupled subduction zones. Phys. Earth Planet. Inter. 54, 258–312. https://doi.org/10.1016/0031-9201(89)90247-1.

Lay, T., Kanamori, H., Ammon, C.J., Hutko, A.R., Furlong, K., Rivera, L., 2009. The 2006-2007 Kuril Islands great earthquake sequence. J. Geophys. Res. 114, B11308. https://doi.org/10.1029/2008JB006280.

Lay, T., Ammon, C.J., Kanamori, H., Rivera, L., Koper, K.D., Hutko, A.R., 2010. The 2009 Samoa-Tonga great earthquake triggered doublet. Nature 466, 964–968. https://doi.org/10.1038/nature09214.

Lay, T., Duputel, Z., Ye, L., Kanamori, H., 2013. The December 7, 2012 Japan Trench intraplate doublet (M_W 7.2, 7.1) and interactions between near-trench intraplate thrust and normal faulting. Phys. Earth Planet. Inter. 220, 73–78.

MacInnes, B.T., Weiss, R., Bourgeois, J., Pinegina, T.K., 2010. Slip distribution of the 1952 Kamchatka great earthquake based on near-field tsunami deposits and historical records. Bull. Seismol. Soc. Am. 100, 1695–1709. https://doi.org/10.1785/0120090376.

Meng, Q., Heeszel, D.S., Ye, L., Lay, T., Wiens, D.A., Jia, M., Cummins, P.R., 2015. The 3 May 2006 (M_W 8.0) and 19 March 2009 (M_W 7.6) Tonga earthquakes: intraslab compressional faulting below the megathrust. J. Geophys. Res., Solid Earth 120, 6297–6316. https://doi.org/10.1002/2015JB012242.

Mueller, S., Spence, W., Choy, G.L., 1996. Inelastic models of lithospheric stress – II. Implications for outer-rise seismicity and dynamics. Geophys. J. Int. 125, 54–72. https://doi.org/10.1111/j.1365-246X.1996.tb06534.x.

Raessi, M., Atakan, K., 2009. On the deformation cycle of a strongly coupled plate interface: the triple earthquakes of 16 March 1963, 15 November 2006, and 13 January 2007 along the Kurile subduction zone. J. Geophys. Res. 114, B10301. https://doi.org/10.1029/2008JB006184.

Satake, K., Baba, T., Hirata, K., Iwasaki, S., Kato, T., Koshimura, S., Takenaka, J., Terada, Y., 2005. Tsunami source of the 2004 off the Kii Peninsula earthquakes inferred from offshore tsunami and coastal tide gauges. Earth Planets Space 57, 173–178.

Seno, T., 2005. The September 5, 2004 off the Kii Peninsula earthquakes as a composition of bending and collision. Earth Planets Space 57, 327–332.

Seno, T., Yamanaka, Y., 1996. Double seismic zones, compressional deep trench-outer rise events and superplumes. In: Bebout, G.E., Scholl, D.W., Kirby, S.H., Platt, J.P. (Eds.), Subduction Top to Bottom. In: Geophys. Monogr., vol. 96. AGU, Washington D.C., pp. 347–355.

Sladen, A., Trevisan, J., 2018. Shallow megathrust earthquake ruptures betrayed by their outer-trench aftershock signature. Earth Planet. Sci. Lett. 483, 105–113. https://doi.org/10.1016/j.epsl.2017.12.006.

Stauder, W., 1968. Mechanism of the Rat Island earthquake sequence of February 1965, with relation to island arcs and sea-floor spreading. J. Geophys. Res. 73, 3847–3858.

Steblov, G.M., Vasilenko, N.F., Prytkov, A.S., Frolov, D.I., Grekova, T.A., 2010. Dynamics of the Kuril-Kamchatka subduction zone from GPS data. Izv. Phys. Solid Earth 46, 440–445.

Taylor, M.A.J., Zheng, G., Rice, J.R., Stuart, W.D., Dmowska, R., 1996. Cyclic stressing and seismicity and strongly coupled subduction zones. J. Geophys. Res. 101 (B4), 8363–8381. https://doi.org/10.1029/95JB03561.

Tichelaar, B.W., Christensen, D.H., Ruff, L.J., 1992. Depth extent of rupture of the 1981 Chilean outer-rise earthquake as inferred from long-period body waves. Bull. Seismol. Soc. Am. 82, 1236–1252.

Tilmann, F.J., Grevemeyer, I., Flueh, E.R., Dahm, T., Goßler, J., 2008. Seismicity in the outer rise offshore southern Chile: indications of fluid effects in crust and mantle. Earth Planet. Sci. Lett. 269, 41–55.

Todd, E.K., Lay, T., 2013. The 2011 Northern Kermadec earthquake doublet and subduction zone faulting interactions. J. Geophys. Res. 118, 1–13.

Ward, S.N., 1983. Body wave inversion: moment tensors and depths of oceanic intraplate bending earthquakes. J. Geophys. Res. 88, 9315–9330.

Wetzler, N., Lay, T., Brodsky, E.E., Kanamori, H., 2017. Rupture-depth-varying seismicity patterns for major and great ($M_W \geq 7.0$) megathrust earthquakes. Geophys. Res. Lett. 44, 9663–9671. https://doi.org/10.1002/2017GL074573.

Ye, L., Lay, T., Kanamori, H., 2012. Intraplate and interplate faulting interactions during the August 31, 2012, Philippine Trench earthquake (M_W 7.6) sequence. Geophys. Res. Lett. 39, L24310. https://doi.org/10.1029/2012GL054164.

Ye, L., Lay, T., Kanamori, H., Rivera, L., 2016. Rupture characteristics of major and great ($M_W \geq 7.0$) megathrust earthquakes from 1990–2015: 1. Source parameter scaling relationships. J. Geophys. Res., Solid Earth 121, 826–844.

Ye, L., Lay, T., Bai, Y., Cheung, K.F., Kanamori, H., 2017. The 2017 Mw 8.2 Chiapas, Mexico, earthquake: energetic slab detachment. Geophys. Res. Lett. 44 (23), 11–824.

Supporting Information for

The 25 March 2020 M_W 7.5 Paramushir, Northern Kuril Islands Earthquake and Major ($M_W \geq 7.0$) Near-Trench Intraplate Compressional Faulting

Lingling Ye[1], Thorne Lay[2], and Hiroo Kanamori[3]

[1] *Guangdong Provincial Key Lab of Geodynamics and Geohazards, School of Earth Sciences and Engineering, Sun Yat-sen University, Guangzhou, China*.

[2] *Department of Earth and Planetary Sciences, University of California Santa Cruz, Santa Cruz, California 95064, USA*.

[3] *Seismological Laboratory, California Institute of Technology, Pasadena, California 91125, USA*.

Contents of this file

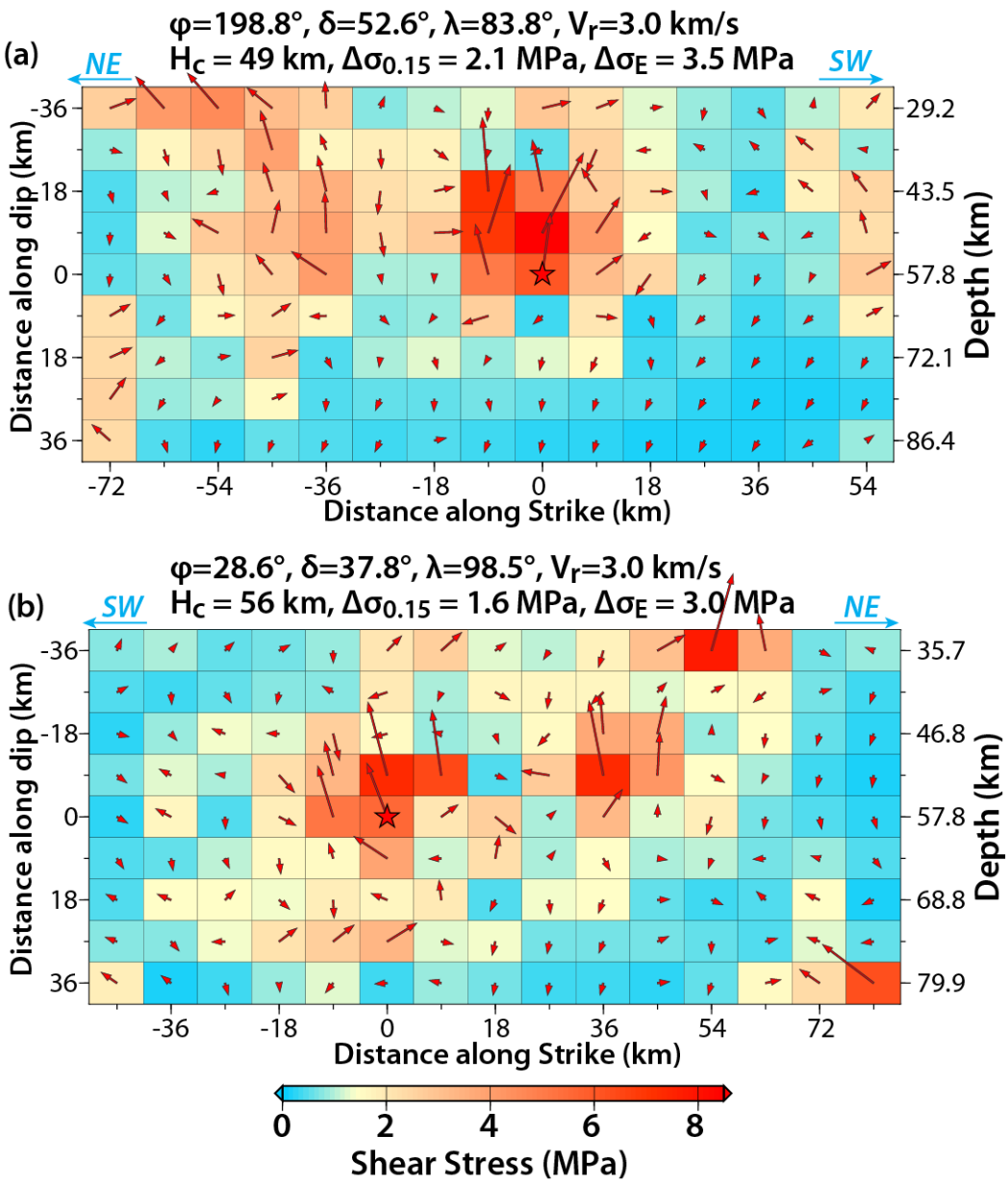

Fig. S1. Stress variations in subfaults on the rupture surface for the inverted slip distributions on the northwest-dipping fault plane in Fig. 1 (a) and southeast-dipping fault plane in Fig. S2 (b), indicated by color scale and with shear stress direction and relative strength indicated by the vectors in each subfault, along with two estimates of the overall static stress drop following the procedure in Ye et al. (2016).

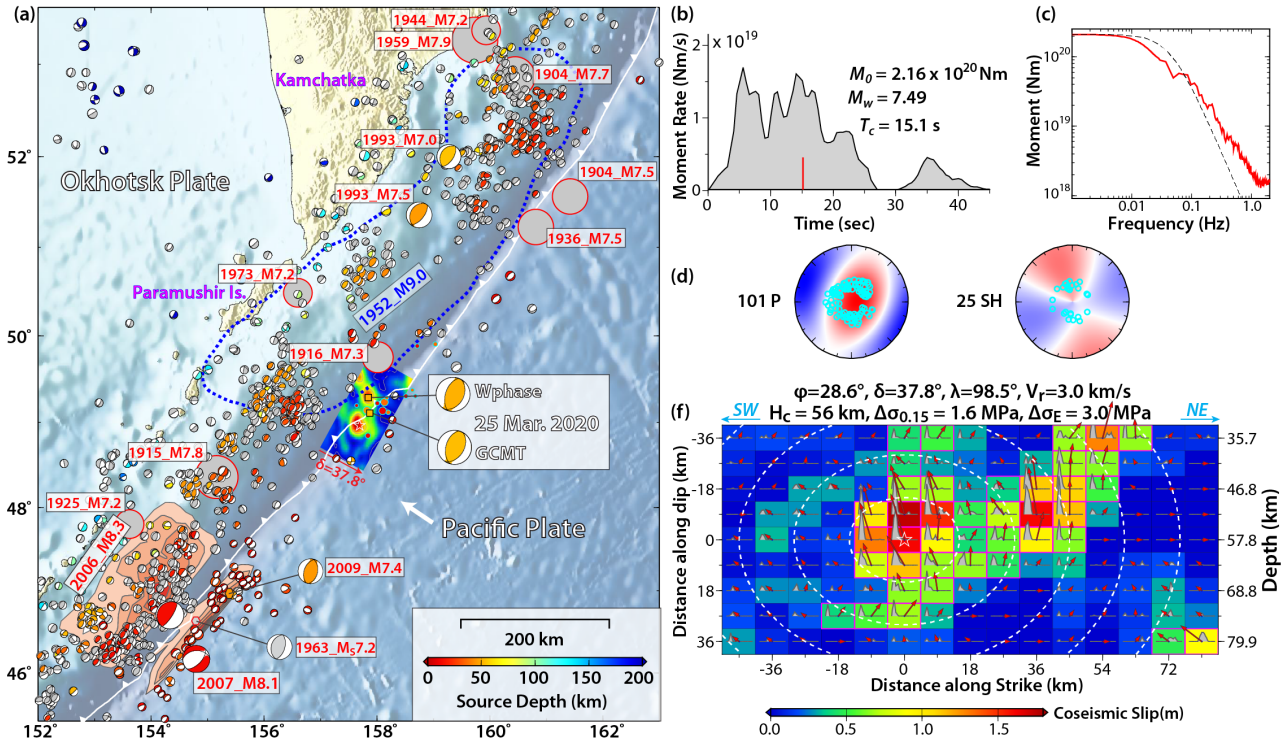

Fig. S2. Rupture location and slip distribution for the 25 March 2020 M_W 7.5 Paramushir, Northern Kuril Islands outer rise compressional earthquake. The slip model is inverted on the southeast-dipping fault plane. Other symbols and the layout are the same as in Fig. 1.

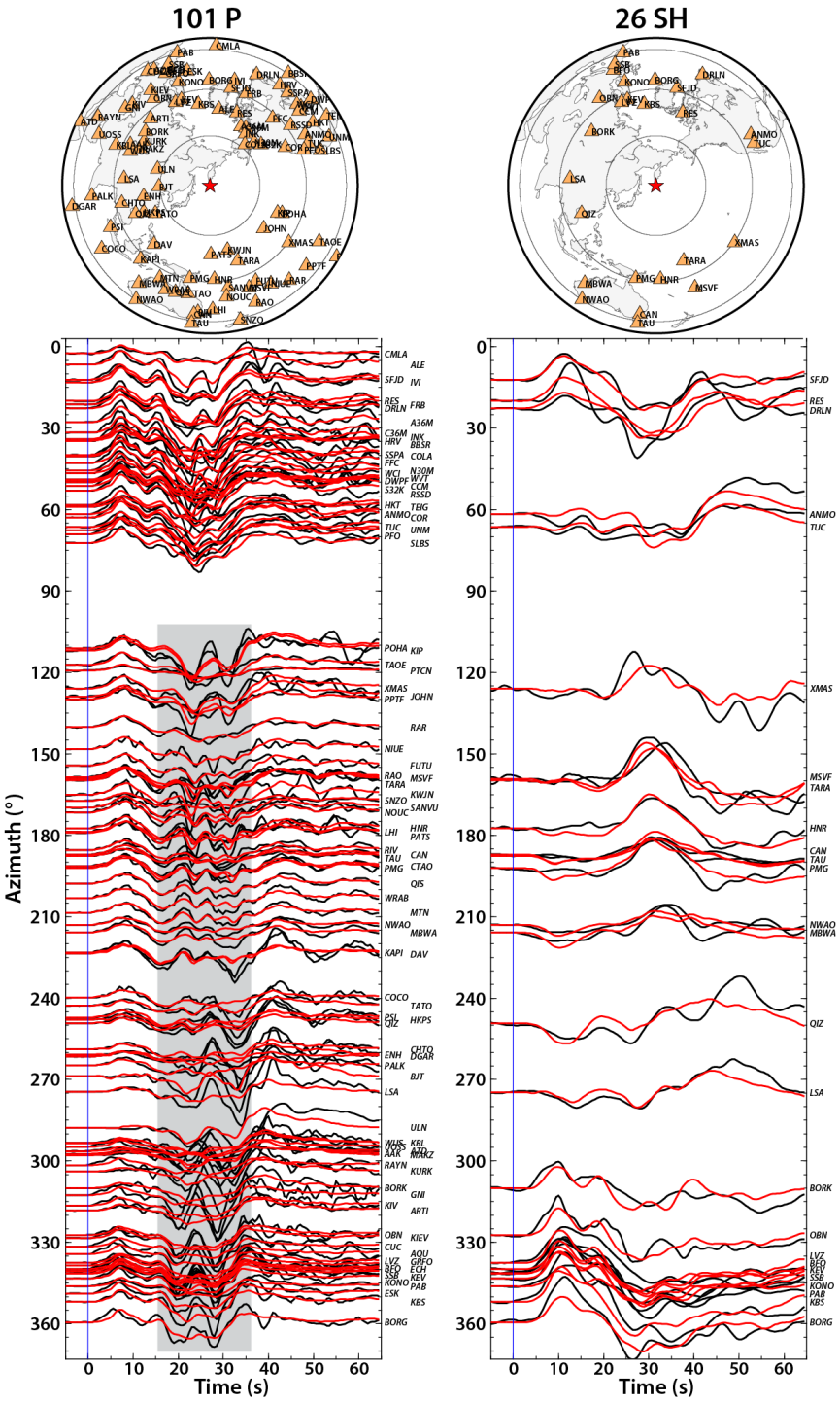

Fig. S3. The azimuthal and distance distribution of the *P* and *SH* wave recordings for the 2020 Paramushir M_W 7.5 earthquake with the observed (black lines) and model predictions (red lines) from the slip model on the southeast-dipping fault plane shown in Fig. S2. The gray rectangle box highlights the relatively poor fitting on depth phases at stations to the west, compared to that from the inverted slip distribution from the northwest-dipping fault plane (Fig. 2).

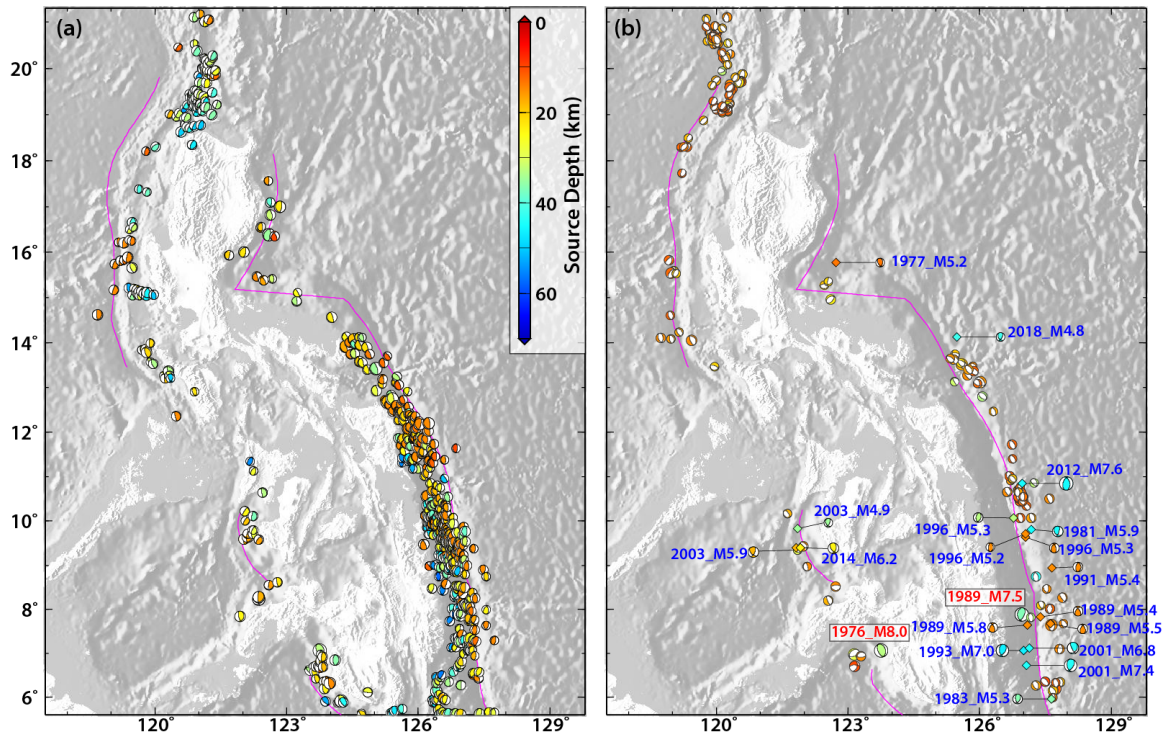

Fig. S4. GCMT mechanisms from 1976-2020 for the subduction zones along the Philippines. Interplate thrust faulting events are shown in (a). Near-trench normal faulting (not labeled), compressional intraplate faulting (blue labels), and large interplate thrust events (red labels) are shown in (b). The moment tensors are color-coded by centroid depth and scaled relative to M_W.

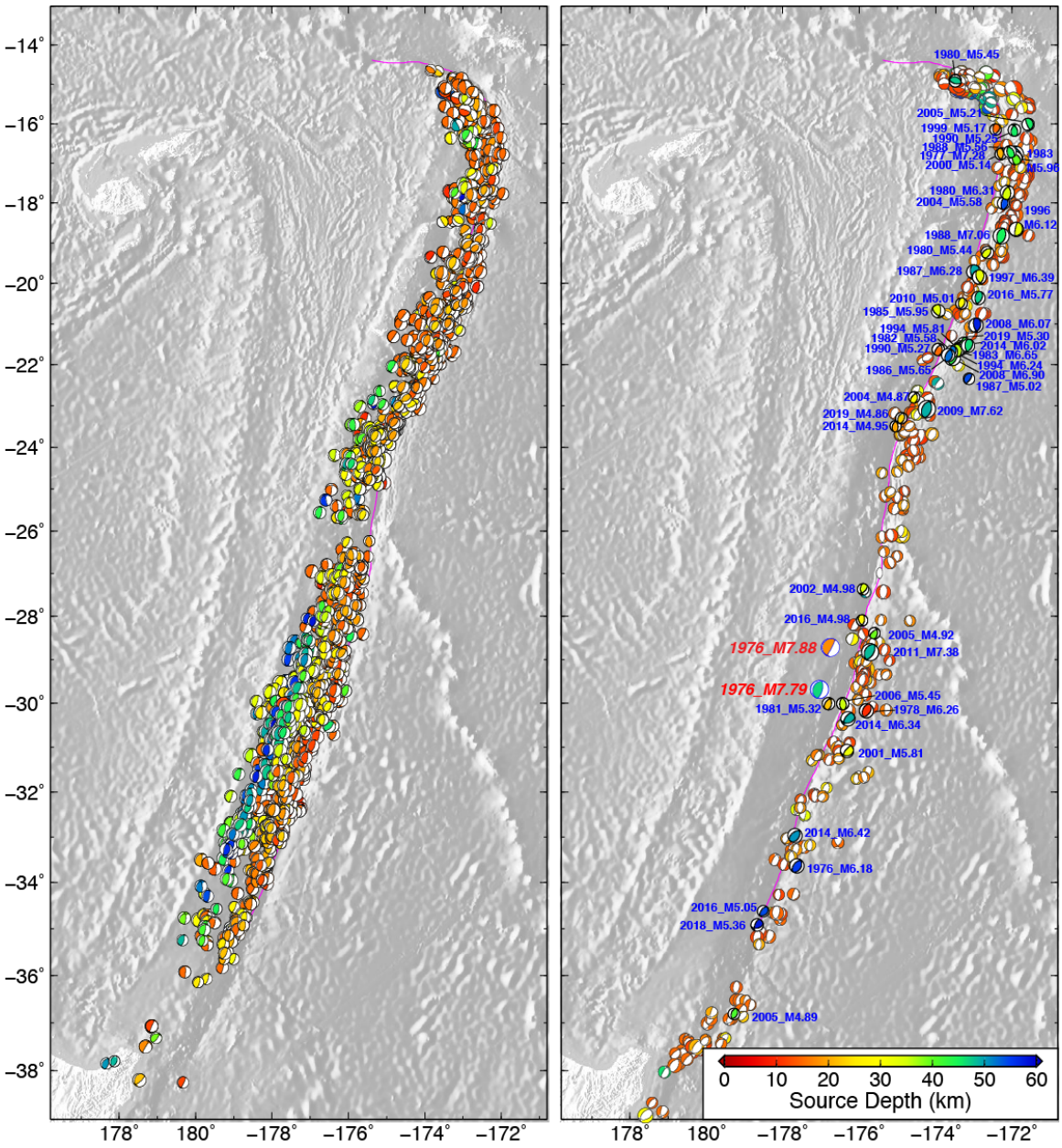

Fig. S5. GCMT mechanisms from 1976-2020 for the subduction zone along Tonga and Kermadec. Interplate thrust faulting events are shown in (a). Near-trench normal faulting (not labeled), compressional intraplate faulting (blue labels), and large interplate thrust events (red labels) are shown in (b). The moment tensors are color-coded by centroid depth and scaled relative to M_W.

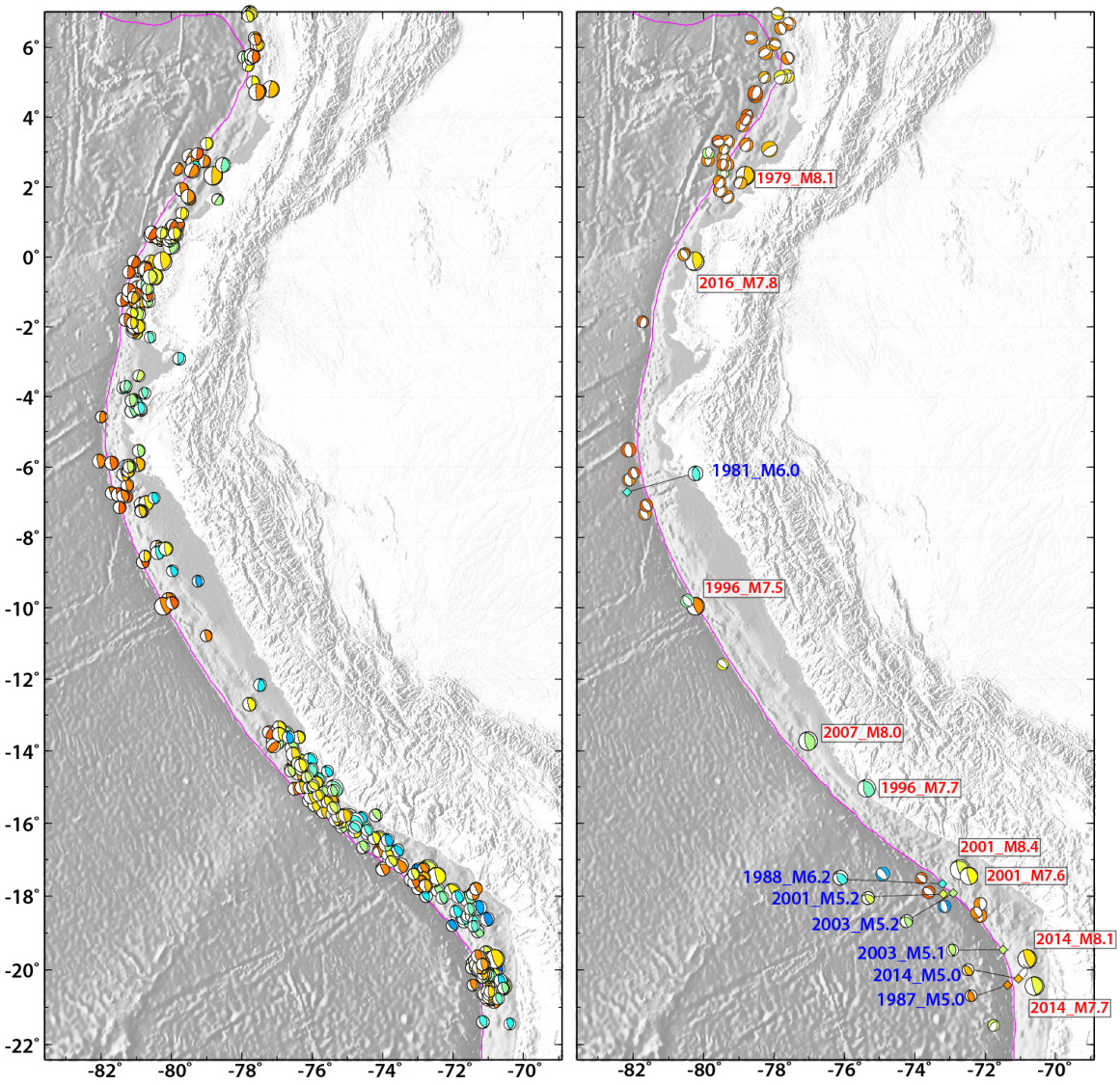

Fig. S6. GCMT mechanisms from 1976-2020 for the subduction zone along Ecuador, Peru and Northern Chile. Interplate thrust faulting events are shown in (a). Near-trench normal faulting (not labeled), compressional intraplate faulting (blue labels), and large interplate thrust events (red labels) are shown in (b). The moment tensors are color-coded by centroid depth and scaled relative to M_W.